

# Numerical study of experimentally inspired stratified turbulence forced by waves

Jason Reneuve,<sup>1</sup> Clément Savaro,<sup>1</sup> Géraldine Davis,<sup>1</sup>  
Costanza Rodda,<sup>1</sup> Nicolas Mordant,<sup>1</sup> and Pierre Augier<sup>1,\*</sup>

<sup>1</sup>*Laboratoire des Écoulements Géophysiques et Industriels,  
Université Grenoble Alpes, CNRS, Grenoble-INP, F-38000 Grenoble, France*

Stratified flows forced by internal waves similar to those obtained in the Coriolis platform (LEGI, Grenoble, France) [1] are studied by pseudospectral triply-periodic simulations. The experimental forcing mechanism consisting in large oscillating vertical panels is mimicked by a penalization method. The analysis of temporal and spatiotemporal spectra reveals that the flow for the strongest forcing in the experiments is composed of two superposed large and quasi-steady horizontal vortices, of internal waves in box modes and of much weaker waves outside the modes. Spatial spectra and spectral energy budget confirm that the flow is in an intermediate regime for very small horizontal Froude number  $F_h$  and buoyancy Reynolds number  $\mathcal{R}$  close to unity. Since the forcing frequency  $\omega_f$  is just slightly smaller than the Brunt-Väisälä frequency  $N$ , there are energy transfers towards slower waves and large vortices, which correspond to an upscale energy flux over the horizontal.

Two other experimentally feasible sets of parameters are investigated. A larger amplitude forcing shows that it would indeed be possible to produce in huge apparatus like the Coriolis platform stratified turbulence forced by waves for small  $F_h$  and buoyancy Reynolds number  $\mathcal{R}$  of order 10. Forcing slower waves for  $\omega_f = 0.40N$  leaves space between  $\omega_f$  and  $N$  for “down-time-scale” transfers through weakly non-linear interactions with temporal spectra consistent with  $\omega^{-2}$  slope. However, for this set of parameters, the large scales of the flow are strongly dissipative and there is no downscale energy cascade.

## I. INTRODUCTION

Statistical results obtained from oceanic measurements are usually interpreted as the signature of an internal wave field. Gravito-inertial waves can propagate into the oceans because of the stable density stratification and the Earth rotation. These two effects are characterized by two frequencies, the Brunt-Väisälä frequency  $N$  and the Coriolis frequency  $f$ , respectively. In the oceans,  $N$  is usually much larger than  $f$ . The velocity and temperature spectra measured at different times and locations were observed to present some similarities. Temporal spectra scale as  $\omega^{-2}$  between the Coriolis frequency  $f$  and the Brunt-Väisälä frequency  $N$ . Vertical spectra tend to scale as  $k_z^{-2}$  at large scales and as  $N^2 k_z^{-3}$  (“saturated spectra”) at intermediate scales. A turbulent  $k^{-5/3}$  slope is observed only at small scales along the vertical (dropped spectra) and at much larger scales along the horizontal (towed

---

\* pierre.augier@univ-grenoble-alpes.fr

spectra). The  $k_z^{-5/3}$  spectrum at small scales corresponds to weakly stratified isotropic turbulence. In contrast, the  $k_h^{-5/3}$  spectrum at much larger scales together with the steeper vertical spectra cannot be due to isotropic turbulence and another interpretation should be found.

Garrett & Munk (GM) [2] showed that a simple model of a continuous superposition of internal waves is consistent with different types of measurements. Even though the GM model is fully empirical and not based on a physical understanding of the underlying dynamics, it is a remarkable result that the oceanic spectra can be modeled with only internal waves, i.e. that the different spectra are consistent with the dispersion and polarization relations. These spectra are often called “wave spectra” but they are actually the footprint of the full dynamics, which can also involve non-wavy flows.

Indeed, flows influenced by stable stratification and system rotation can also contain a non-wavy “balanced” part [3]. For example, in the case without rotation, the equation for the vertical vorticity  $\omega_z$  does not contain any linear terms, which implies that the so-called “horizontal vortices” (associated with  $\omega_z$  and horizontal velocity) are not linearly coupled with the buoyancy. In the large majority of recent numerical simulations of stratified turbulence, the associated “vortical” (more precisely toroidal) energy is not small and horizontal vortices play a key role. Moreover, wave-vortex interactions appear to be more efficient than wave-wave interactions to drive a forward cascade [4].

There had been a lot of debate about the dynamical regime producing the GM spectra and different physical explanations have been proposed (for reviews, see [4, 5]). The success of the GM model seems to indicate that the oceanic spectra are due to a kind of internal wave turbulence. However, such spectra have not been reproduced with internal waves, neither with laboratory experiments nor with numerical simulations. The large-scale  $k_h^{-5/3}$  spectrum tends to indicate that there could be an anisotropic turbulent cascade with an energy flux through the horizontal scales. Recently, the theory of Weak Wave Turbulence (WWT), which assumes that the flow consists only of weakly interacting waves, has been used to derive solutions corresponding to the standard GM spectra and to observed variabilities around this historical model [5, 6].

An alternative dynamical explanation of the oceanic spectra has been proposed by Lindborg, Brethouwer and Riley [7, 8]. They show that many oceanic measurements could actually be compatible with “strongly stratified turbulence” [9, 10]. This regime is strongly nonlinear and involves, similarly to isotropic turbulence, both toroidal (associated with  $\omega_z$ ) and poloidal, horizontally divergent, modes. In the inertial range, the energy is approximately equipartitioned between these two modes. We will follow [11] and call this particular regime “LAST” (for Layered Anisotropic Stratified Turbulence) to avoid confusion with other somehow turbulent regimes in stratified fluids. The LAST regime is associated with a downscale energy cascade and is obtained only when the large scales are simultaneously strongly stratified (small horizontal Froude number  $F_h$ ) and weakly influenced by viscosity (large buoyancy Reynolds number  $\mathcal{R} = ReF_h^2$ ) [12].

Flows in the LAST regime have been obtained in high resolution idealized simulations. In contrast, we are not aware of studies reporting forced dissipative flows composed of a continuum of internal waves (without vortical modes) associated with spectra similar to oceanic ones. Let us note that reproducing this regime might require very large experimental apparatus or very large simulations that were until recently unfeasible. Moreover, most

numerical simulations of stratified turbulence were not designed to produce a pure internal wave field without vortices, as described in the GM models. We can mention few studies focussing on this subject.

- Waite & Bartello [4] carried out simulations of stratified turbulence forced in waves with  $k_z \sim k_h$  (fast waves for which  $\omega \simeq 0.7N$ ). They concluded that they have been unsuccessful at reproducing the observed spectra and that the effects of adding vortices can be dramatic.
- Lindborg & Brethouwer [9] completed this study by forcing in waves with  $k_z \gg k_h$  (slow waves for which  $\omega \ll N$ ) such that the vertical Froude number  $F_v = UN/l_v$  is of order unity. For some parameters, they observed a clear downscale energy cascade. Their spatial and spatiotemporal spectra show that the dynamics of the inertial range corresponds to the LAST regime and that inertial waves dominate only for the very large horizontal scales.
- Le Reun *et al.* [13] simulate some forced dissipative flows made of internal gravity waves but the buoyancy Reynolds number is quite small. Therefore, these waves should be dissipated at large horizontal scales and there is no need for a downscale energy cascade bringing energy at small horizontal scales.
- Calpe Linares *et al.* [14] studied two-dimensional stratified turbulence forced by fast internal waves. They verified that the conditions on  $F_h$  and  $\mathcal{R}$  also determined the regime for 2d stratified turbulence. For values corresponding to the oceanic dynamics ( $F_h \ll 1$  and  $\mathcal{R} \gg 1$ ), the dynamics corresponds to a strongly nonlinear regime which cannot be interpreted in the framework of the WWT theory.

Recent experiments [1, 15] have managed to generate strongly stratified turbulent flows by forcing large scale internal waves into a large scale tank (the Coriolis platform in Grenoble) filled with stratified salty water. A continuum of waves was observed, and key elements of WWT phenomenology were identified. However, some discrepancies with the phenomenology were noticed, such as a flat frequency spectra or finite size effects in the form of resonant modes. Frequency spectra qualitatively consistent with GM spectra were observed at frequencies greater than the forcing and extending at frequencies greater than  $N$ . This observation suggests the occurrence of strongly non linear wave turbulence [15].

In this article, we present the results of numerical simulations that were designed in direct inspiration of the experiments of [1]. In particular, we model with a immersed boundary method the experimental forcing mechanism which uses oscillating panels on the boundaries of the fluid domain to generate waves. This forcing scheme is uncommon for numerical simulations, as it is local in space and forces only waves, as opposed to most numerical forcing schemes used in stratified turbulence. We focus in this study on sets of physical parameters that were or could be obtained in real experiments in huge apparatus like the Coriolis platform. The paper is not aimed at simulating the details of the experiment but only its major characteristics.

This article is organized as follow. The numerical methods are presented in section 2. Section 3 is dedicated to the analysis of simulations corresponding to a set of parameters considered in [1]. We then extend in section 4 the experiments of [1] by considering two other sets of parameters that could be obtained in the Coriolis platform.

## II. NUMERICAL SETUP

The numerical simulations presented in this article are performed using the pseudospectral solver `ns3d.strat` from the FluidSim Python package [16–18]. The simulations and the analysis should be reproducible with Fluidsim version 0.6.1 [19]. Using this solver, we integrate the three-dimensional Navier-Stokes equations under the Boussinesq approximation with an added fourth-order hyperviscosity term:

$$\partial_t \mathbf{v} + (\mathbf{v} \cdot \nabla) \mathbf{v} = b \mathbf{e}_z - \frac{1}{\rho_0} \nabla p + \nu_2 \nabla^2 \mathbf{v} + \nu_4 \nabla^4 \mathbf{v} + \mathbf{f}_h, \quad (1)$$

$$\partial_t b + (\mathbf{v} \cdot \nabla) b = -N^2 v_z + \kappa_2 \nabla^2 b + \kappa_4 \nabla^4 b, \quad (2)$$

where  $\mathbf{v}$  is the velocity,  $p$  the pressure,  $b = -g\delta\rho/\rho_0$ , with  $\rho_0$  the mean density and  $\delta\rho$  the departure from the stable linear density stratification. For all simulations, the second-order viscosity is set to the value for water in usual temperature and pressure conditions,  $\nu_2 = 10^{-6} \text{ m}^2/\text{s}$ . In the following, all physical quantities from simulation data are expressed in SI units.

The fourth-order viscosity  $\nu_4$  is left as a free parameter and adapted to the resolution of simulations in order to ensure that the energy brought at the smallest simulated scales by the non linear fluxes are dissipated without accumulation. Similarly, the equation of motion (2) for the buoyancy field  $b$  presents both second and fourth order diffusive terms, with corresponding diffusion coefficients  $\kappa_2$  and  $\kappa_4$ . We can then build two different Prandtl numbers  $\text{Pr}_i = \nu_i/\kappa_i$  for  $i = 2, 4$ . In all simulations, both those Prandtl numbers are set to unity, such that  $\kappa_2 = \nu_2$  and  $\kappa_4 = \nu_4$ . The use of both normal and hyperviscosity is an important tool for the comparison with experiments. It allows us to carry out simulations with a well defined physical Reynolds number at a coarse resolution and to be able to quantify the difference with a proper DNS. More specifically, we use the measure of the turbulent kinetic dissipations  $\varepsilon_{K2}$  and  $\varepsilon_{K4}$  based on both viscosities, and the ratio  $\varepsilon_{K2}/\varepsilon_K$  where  $\varepsilon_K = \varepsilon_{K2} + \varepsilon_{K4}$  is the total kinetic energy dissipation, as an indicator of how close the simulations we perform are to proper DNS of the true Navier-Stokes equations with only water viscosity. For a set of physical parameters, the needed hyperviscosity decreases when the resolution is increased and the ratio  $\varepsilon_{K2}/\varepsilon_K$  grows towards unity.

The geometry and forcing scheme used for the simulations are inspired by the configuration of experiments that were performed in the Coriolis facility in LEGI, Grenoble (France) [1]. In the experiments, a parallelepipedic domain of size  $6 \times 6 \times 1 \text{ m}^3$  is isolated inside the tank of the facility, using two adjacent fixed walls and two oscillating walls acting as wavemakers. The wavemakers are set to oscillate around their mid-height horizontal axis, with frequency  $\omega_f$  and maximum horizontal excursion  $a$  being free parameters of this forcing mechanism. In the simulations we present here, the wavemakers are modeled using a  $L^2$  volume penalization method [20, 21], which is schematized in figure 1.

This penalization methods works by introducing a forcing term of the following shape in the momentum equation (1):

$$\mathbf{f}_h = \frac{1}{\tau} \Theta(\mathbf{x})(\mathbf{v}_h^*(\mathbf{x}, t) - \mathbf{v}_h), \quad (3)$$

where  $\mathbf{v}_h^*(\mathbf{x}, t)$  is the target velocity profile imposed by the wavemakers,  $\Theta(\mathbf{x})$  is an activation function ensuring that the forcing acts only locally in place of the wavemakers, and  $\tau$  is a

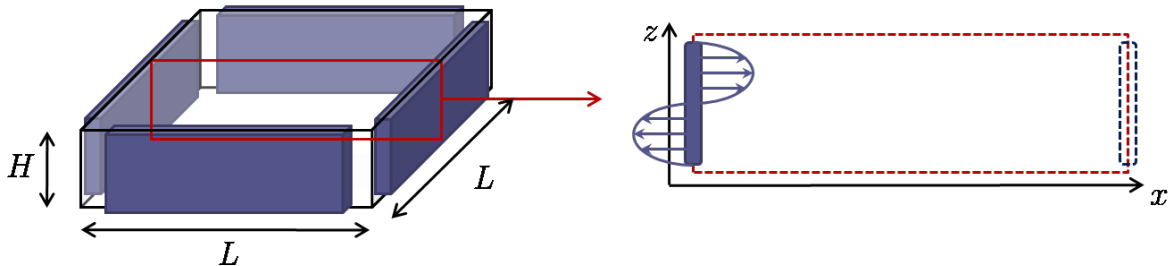


FIG. 1. Schematic representation of the  $L^2$  volume penalization method, shown in the whole simulation domain (left) and in a vertical cut (right). Wavemakers are modeled by parallelepipedic penalization volumes (in dark blue) close to the vertical boundaries of the simulation domain. In each of these volumes, we implement a virtual body force designed to impose a prescribed velocity profile (blue arrows) on the normal component of the fluid velocity field. The vertical periodicity of the simulation domain is ensured by choosing a sinusoidal velocity profile with one wavelength over the height  $H$  of the box. Horizontal periodicity is ensured by having the penalization volumes sit over the vertical boundaries of the domain, so that facing boundaries are imposed the same velocity profile at all times. The mathematical details of the virtual body force are given in equation (3).

typical timescale at which the forcing acts. The forcing term described by equation (3) ensures that in the region where  $\Theta(\mathbf{x}) = 1$ , the horizontal velocity field  $\mathbf{v}_h$  follows the target velocity  $\mathbf{v}_h^*$  over timescales that are large compared to  $\tau$ . In order to give a meaningful description of the dynamics imposed by wavemakers, we must then choose  $\tau$  to be small compared to the typical timescales of the flow that we simulate. Typically, we take  $\tau$  to be small compared to the Brunt-Väisälä period, i.e.  $\tau = T_N/20$ , with  $T_N = 2\pi/N$ . The activation function  $\Theta(\mathbf{x})$  is zero outside the wavemakers, and unity inside a region representing the oscillating panels. For the sake of simplicity, we choose this activation region of a single panel to be a parallelepiped of the same height as the simulation domain, of length slightly smaller than the horizontal size of the box in order to avoid interpenetration of the panels in the corners, and with a thickness equal to the forcing amplitude  $2a$ . In order to ensure the horizontal periodicity of the forcing term  $\mathbf{f}$  that is required by the pseudospectral solver, the activation region of each panel is centered on the corresponding vertical boundary of the box, meaning that contrary to the experimental setup, the panels are not facing motionless walls but rather a virtual copy of themselves. Additionally to the periodicity constraint, the use of a pseudospectral solver requires that the activation function  $\Theta$  is a smooth function of space in order to avoid Gibbs oscillations. To ensure this, we take  $\Theta$  to grow from zero to unity as a hyperbolic tangent when crossing the activation region boundary, over a small scale set arbitrarily to four grid points. Inside the activation region of each wavemaker, we apply the forcing term only to the fluid velocity component that is orthogonal to the corresponding vertical boundary, meaning that we model the panels with a free-slip boundary condition, and that we neglect their vertical motion. This last approximation is justified by the fact that the experimental values for  $a$  are of the order of a few centimeters, meaning that the angular excursion of a panel is very small. We thus only prescribe the orthogonal component of the target velocity field to be  $v_\perp^* = a \sin(2\pi z/L_z) s(t)$ , with  $L_z$  the height of the simulation box, and  $s(t)$  a prescribed

temporal forcing signal. The sinusoidal shape ensures that the prescribed velocity field is periodic vertically. Let us note that as a consequence, here the panels force modes with one vertical wavelength, as opposed to the experimental setup where the wavemakers force modes with half a vertical wavelength. In order to have modes with the same wavelengths as in the experiments, and to keep the same aspect ratio  $L_x/L_z = L_y/L_z = 6$ , we then double the size of the numerical domain, effectively performing simulations in a box of size  $12 \times 12 \times 2 \text{ m}^3$ . Finally, the time signal  $s(t)$  of the forcing oscillates at a frequency  $\omega_f = FN$ , which is randomly modulated in time in a narrow band of width 10% as was done in the experiment. At the beginning of every simulation, two realizations of the forcing time signal are generated, one for each pair of facing wavemakers. By doing so, we make sure that the phases of adjacent wavemakers stay uncorrelated in time. This forcing scheme corresponds to the Fluidsim parameter `params.forcing.type="watu_coriolis"` and is implemented in the module `fluidsim/solvers/ns3d/forcing/watu.py`.

For all simulations we take  $N = 0.6 \text{ rad/s}$  and  $\nu_2 = 10^{-6} \text{ m}^2/\text{s}$ . The remaining free parameters are the resolution  $n_x \times n_y \times n_z$ , the reduced forcing frequency  $F \equiv \omega_f/N$  and the amplitude  $a$ . The hyperviscosity  $\nu_4$  is adapted to the other parameters so that the dissipative scales are well-resolved. The simulations were performed on a local cluster at LEGI for resolutions up to  $480 \times 480 \times 80$ , and on the national CINES cluster Occigen for resolutions up to  $2304 \times 2304 \times 384$ . Parameters and dimensionless numbers for each simulations are summarized in table I. The turbulent nondimensional numbers are computed from the statistically stationary flows as  $F_h = \varepsilon_K/(U_h^2 N)$  and  $\mathcal{R}_2 = \varepsilon_K/(\nu_2 N^2)$ , where  $\varepsilon_K$  is the mean kinetic energy dissipation and  $U_h$  the rms horizontal velocity. The results presented in this article are obtained from periods of the simulation when a steady state has been approximately reached. Because the time scales of the flows studied here are very long, finding such steady-state period can be very difficult and computationally costly. In order to reach an approximately steady state in a reasonable time, we start all the simulations at a reduced resolution  $240 \times 240 \times 40$ , and increase the resolution step by step only when a sufficiently stationary state has been reached. When such a state is observed, specific outputs are turned on and the simulation is ran further for 10 to 20 minutes of equation time in order to produce substantial data to analyze, before increasing the resolution again if needed.

Figure 2 summarizes the successive runs and resolution changes since the beginning of the simulation for  $F = \omega_f/N = 0.73$  and  $a = 5 \text{ cm}$ . We see that most of the equation time is taken by the initial transient state from a static initial condition, which justifies the use of smaller resolutions for the simulation of transient states, as it is faster and less computationally expensive. Indeed, the first transient between  $t_0$  and  $t_1$  takes up most of the equation time but is computed in a few hours on a local cluster at resolution  $240 \times 240 \times 40$ , whereas the last period of data analysis from  $t_4$  to  $t_{\text{end}}$  represent a small amount of equation time but requires days of computation on the national cluster Occigen.

In the following sections, results are presented for the resolutions  $480 \times 480 \times 80$ ,  $1152 \times 1152 \times 192$  and  $2304 \times 2304 \times 384$ . Snapshots of the buoyancy field are shown in figure 3 for resolutions  $480 \times 480 \times 80$ ,  $1152 \times 1152 \times 192$  and  $2304 \times 2304 \times 384$ . The snapshots show clear anisotropy confirming that the flow is strongly affected by gravity. We see that small scales appear only for the two largest simulations, which is consistent with the values of  $\eta k_{\text{max}}$  given in the 3 first lines of table I. In the following, the results of the simulations with the

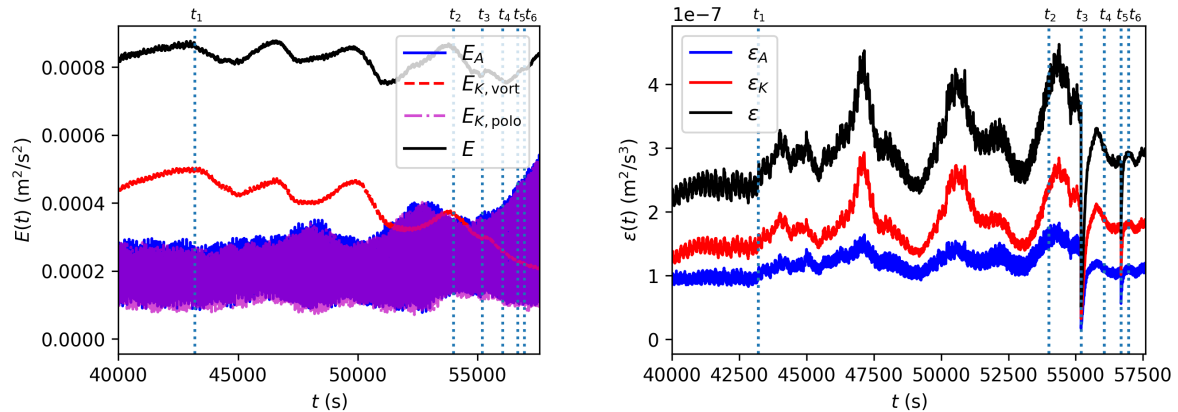


FIG. 2. Time evolution of the energy components (left) and dissipation (right) for parameters  $F = 0.73$  and  $a = 5$  cm, since the beginning of the initial run. Vertical dotted lines signal the initial time  $t_i$  of each successive run, for  $i = 0, \dots, 4$ . The simulations first runs at resolution  $240 \times 240 \times 40$  between  $t_0 = 0$  s and  $t_1 = 43200$  s. At  $t = t_1$  the resolution is increased to  $480 \times 480 \times 80$  and the simulation runs until  $t_2 = 54000$  s. At  $t = t_2$ , temporal and spatiotemporal outputs are turned on and the simulation runs until  $t_3 = 55200$  s for analysis. At  $t = t_3$ , the resolution is increased to  $1152 \times 1152 \times 192$  and the simulation runs with outputs off until  $t_4 = 56058$  s. At  $t = t_4$  outputs are turned back on and the simulation runs until  $t_5 = 56684$  s for analysis. At  $t = t_5$ , outputs are turned off, the resolution is increased a last time to  $2304 \times 2304 \times 384$  and the simulation runs until  $t_6 = 56972$  s. Finally from  $t = t_6$  to  $t_{\text{end}} = 57598$  s the simulation runs with outputs on for analysis.

coarser resolution are used only when more statistics are needed for a better convergence.

Throughout this article, we make an extensive use of the poloidal/toroidal decomposition [22, 23] also known as the Craya-Herring decomposition [24, 25]. This decomposition consists in separating the horizontal velocity field into a horizontally divergent part  $\mathbf{v}_{hd}$  and a part  $\mathbf{v}_{hr}$  carrying the vertical vorticity:

$$\mathbf{v} = \mathbf{v}_z + \mathbf{v}_h = \mathbf{v}_z + \mathbf{v}_{hd} + \mathbf{v}_{hr}, \quad (4)$$

where  $\nabla \cdot \mathbf{v}_h = \nabla \cdot \mathbf{v}_{hd}$  and  $\mathbf{e}_z \cdot (\nabla \times \mathbf{v}_h) = \mathbf{e}_z \cdot (\nabla \times \mathbf{v}_{hr})$ . In Fourier space, this decomposition becomes simple when expressed in the cylindrical basis  $(\mathbf{e}_h, \mathbf{e}_\theta, \mathbf{e}_z)$  around axis  $z$ :

$$\hat{\mathbf{v}} = \hat{v}_z \mathbf{e}_z + \hat{v}_{hd} \mathbf{e}_h + \hat{v}_{hr} \mathbf{e}_\theta. \quad (5)$$

This decomposition is thus conveniently performed by projecting the horizontal velocity field in Fourier space on the radial and azimuthal unit vectors  $\mathbf{e}_h$  and  $\mathbf{e}_\theta$ , respectively. Since the cylindrical basis is orthogonal, the kinetic energy can also be decomposed in the same fashion:

$$E_K = E_{Kz} + E_{Khd} + E_{Khr}. \quad (6)$$

In technical terms, the velocity components are regrouped into a poloidal field  $\mathbf{v}_p = \mathbf{v}_z + \mathbf{v}_{hd}$ , associated with poloidal energy  $E_{Kp} = E_{Kz} + E_{Khd}$  and a toroidal field  $\mathbf{v}_t = \mathbf{v}_{hr}$  accounting

$F$	$a$ cm	$n_x \times n_y \times n_z$	$\nu_4$ m <sup>4</sup> /s	$F_h$	$\mathcal{R}_2$	$\Gamma$	$\eta k_{\max}$	$\varepsilon_{K2}/\varepsilon_K$
0.73	5	480×480×80	3.86e-08	7.87e-04	0.68	0.64	0.12	0.13
0.73	5	1152×1152×192	6.39e-10	6.70e-04	0.49	0.59	0.44	0.47
0.73	5	2304×2304×384	1.2e-11	6.52e-04	0.49	0.59	0.88	0.87
0.73	10	480×480×80	1.11e-07	1.89e-03	5.06	0.74	0.07	0.05
0.73	10	1152×1152×192	1.28e-09	2.20e-03	6.26	0.60	0.23	0.17
0.73	10	2304×2304×384	1.85e-10	2.33e-03	6.60	0.57	0.46	0.29
0.45	10	480×480×80	2.18e-08	5.89e-04	0.48	0.91	0.13	0.19
0.40	10	480×480×80	2.18e-08	4.10e-04	0.22	0.54	0.16	0.23
0.40	10	1152×1152×192	6.18e-10	5.81e-04	0.31	0.52	0.49	0.48
0.40	10	2304×2304×384	2.65e-11	5.85e-04	0.33	0.54	0.96	0.76

TABLE I. Summary of the simulations. For all simulations,  $L_z = \lambda_{fz} = 2$  m,  $L_x = L_y = 12$  m,  $N = 0.6$  rad/s and  $\nu_2 = 10^{-6}$  m<sup>2</sup>/s are fixed. The first four columns contain the simulations control parameters which are the normalized forcing frequency  $F = \omega_f/N$ , the forcing amplitude  $a$ , the resolution  $n_x \times n_y \times n_z$  and the hyperviscosity  $\nu_4$ . The last five columns contain important dimensionless numbers such as the horizontal Froude number  $F_h$ , buoyancy Reynolds number  $\mathcal{R}_2$ , the mixing coefficient  $\Gamma = \varepsilon_A/\varepsilon_K$  (with  $\varepsilon_A$  the available potential energy dissipation rate) and the dissipation ratio  $\varepsilon_{K2}/\varepsilon_K$ . All dimensionless numbers are computed from turbulent quantities and averaged in time over a statistically stationary period.

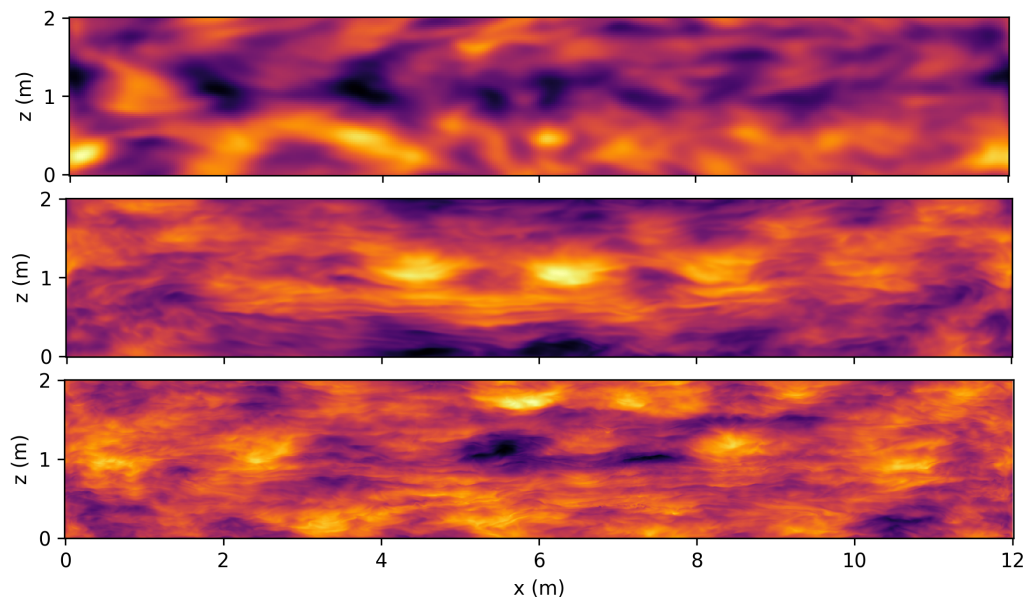


FIG. 3. Buoyancy field snapshots from three successive runs for  $F = 0.73$  and  $a = 5$  cm. Top: taken at  $t_3 = 55200$  s, resolution is  $480 \times 480 \times 80$ . Middle: taken at  $t_5 = 56684$  s, resolution is  $1152 \times 1152 \times 192$ . Bottom: taken at  $t_{\text{end}} = 57598$  s, resolution is  $2304 \times 2304 \times 384$ . All snapshots are vertical slices in the middle of the numerical domain at  $x = 6$  m.



for toroidal energy  $E_{Khr}$ . To help nonspecialist readers, in the following we will not use the word toroidal and we will prefer "vortical" (associated with vertical vorticity). This rearrangement of the velocity components is meaningful in stratified turbulence. First, one can see by considering the inviscid equation for the vertical vorticity

$$\partial_t \omega_z + \mathbf{v} \cdot \nabla \omega_z = \boldsymbol{\omega} \cdot \nabla v_z \quad (7)$$

that this part of the flow is not directly influenced by a linear term related to buoyancy and has therefore no wavy behavior. Second, for weak nonlinearity levels, the poloidal component can be identified as being mostly waves.

A typical aspect of triply periodic numerical simulations of stratified turbulence is the uncontrolled growth of so-called shear modes, which are modes of the horizontal velocity with no horizontal structures [9, 26, 27]. In Fourier space, these modes correspond to  $\hat{\mathbf{v}}_{hr}(k_x = 0, k_y = 0, k_z)$ . Although these modes can play an important role in the overall flow dynamics [28], they are absent from the experiments in [1] as half of the vertical walls of the tank are immobile, thus imposing a hard boundary condition on the horizontal velocity field and preventing any horizontally-averaged horizontal flow. In order to stay as reasonably close as possible to the experiments, we decided to prevent shear modes altogether by imposing  $\hat{\mathbf{v}}_{hr}(0, 0, k_z) = 0$  at all times [29].

Similarly to shear modes, fast waves oscillating at  $\omega = N$  are absent from the experiments. These waves oscillate vertically with no vertical structure, i.e. they correspond in Fourier space to  $\hat{v}_z(k_x, k_y, 0)$ . As a consequence, they are prevented from the experiments by the hard boundary condition at the bottom of the tank where velocity must be zero at all times. In our periodic simulations, those waves have no reason to vanish and can actually be observed with significant energy levels compared to waves in the frequency range just below  $N$ . For the sake of the comparison with experiments, we proceed as for shear modes and impose  $\hat{v}_z(k_x, k_y, k_z = 0) = 0$  in all the following simulations [30].

### III. SIMULATIONS FOR $N = 0.6$ RAD/S, $F = 0.73$ AND $a = 5$ CM

We present in this section a first set of simulations for parameters ( $N = 0.6$  rad/s,  $F = \omega_f/N = 0.73$  and  $a = 5$  cm) corresponding to the experiment with the largest amplitude described in [1]. For this experiment, the strong mixing of salt in the tank prevented the full usage of imaging techniques. By starting with this experimental set of parameter, we thus intend to give a complementary vision to what was done in [1].

#### A. Time evolution of energy and dissipation terms

Figure 4 shows the evolution of energy components and dissipation over the period of time that was selected for data analysis for the resolution  $2304 \times 2304 \times 384$ . It corresponds to 10 minutes of equation time. For the coarser resolutions  $1152 \times 1152 \times 192$  and  $480 \times 480 \times 80$ , we average on 10 and 20 minutes, respectively. In comparison, the experiments described in [1] ran for five hours, and temporal analysis such as temporal spectra were performed using a Welch method with a 20 minutes long temporal window. We see that over the selected periods the statistical stationarity of the system is not perfect, as long-time drifts are still

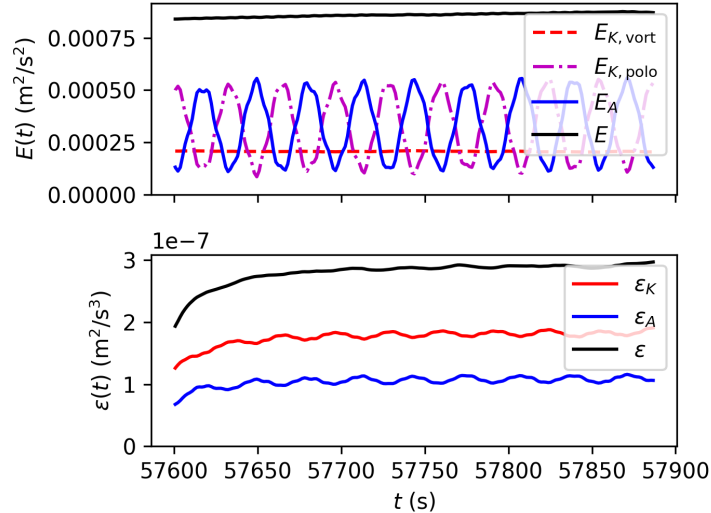


FIG. 4. Time evolution over a statistically stationary period of the energy components (top row) and dissipation (bottom row) for parameters  $F = 0.73$ ,  $a = 5$  cm and for  $2304 \times 2304 \times 384$ .

observable, for example in the total energy and dissipations (black lines). However, as suggested by figure 2 and because of the length of the time scales that are at play, obtaining a more meaningful statistical stationarity would require to run the simulation and output data on a period of equation time that is not computationally reasonable. Therefore, the size of the time window that we selected for further analysis is the result of a compromise between statistical stationarity, time resolution of the specific data outputs, and computational time. Looking into the detail of energy components in figure 4 (top row), we see that kinetic poloidal and potential energy present well-defined, antiphase oscillations around the same average level, suggesting the presence of stationary waves in the simulation box as were seen in the experiment [1]. The remaining kinetic energy is vortical energy (associated with vortices with purely horizontal velocity), which is slightly smaller than the averaged poloidal energy.

## B. Representations of the flow in physical space

A snapshot of the flow is displayed in figure 5. We clearly see a check pattern in the buoyancy field represented by the colors. This corresponds to the large scale forced waves. However, the pattern is deformed and there are weak smaller scale structures in some regions. In contrast, the horizontal velocity field represented by the arrows is dominated by a very large vortex.

A time-averaged, horizontal cross-section of the velocity field from the run in  $1152 \times 1152 \times 192$  (figure 6, left) shows a large, horizontal vortex centered in the middle of the simulation box. It is worth noting that a similar vortex can be observed in experiments, as shown on the right panel of figure 6. We see that velocity magnitudes differ by approximately a factor 3 between simulation and experiment, though it should be noted first that the experimental field was acquired one hour after the beginning of the experiment, compared

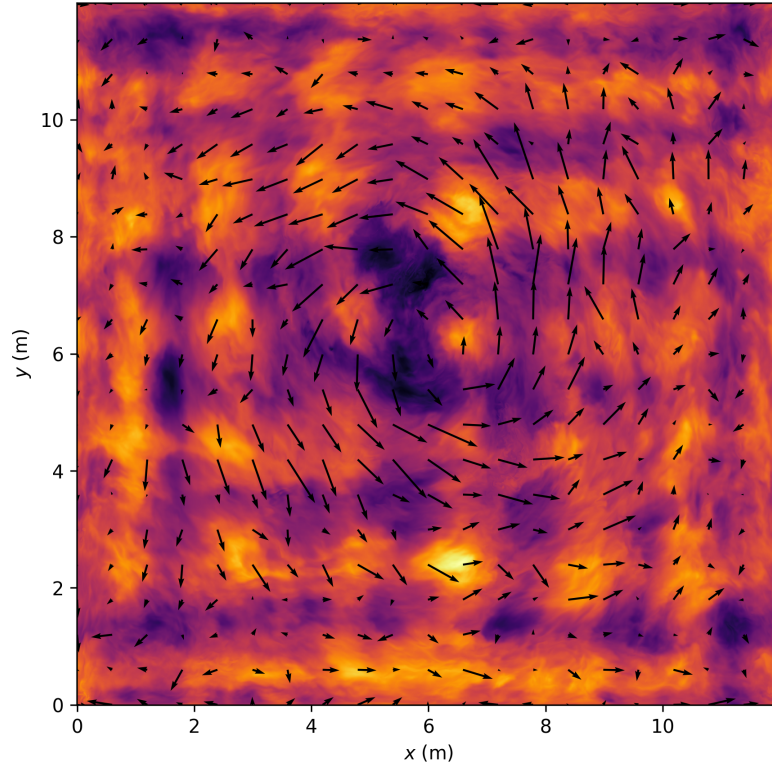


FIG. 5. Horizontal cross-section for  $F = 0.73$  and  $a = 5$  cm ( $2304 \times 2304 \times 384$ ). The colors and the vector represent the buoyancy field and the velocity field, respectively.

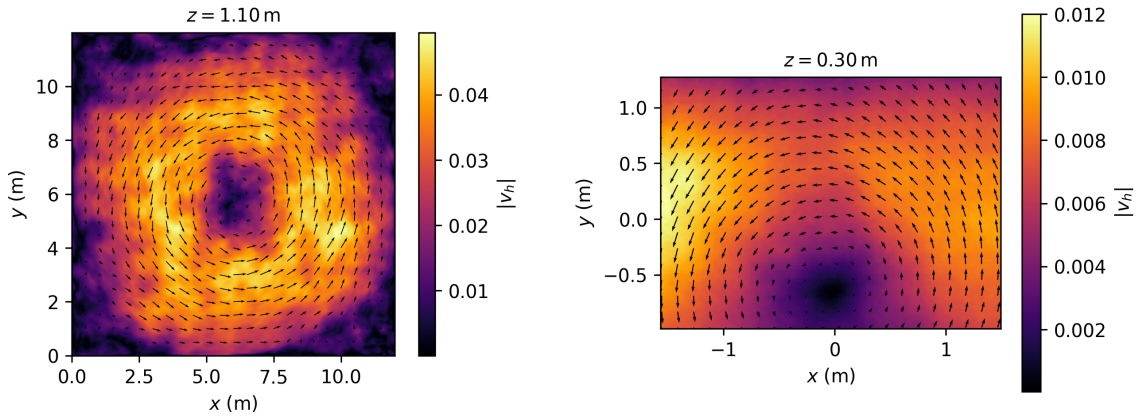


FIG. 6. Time-averaged, horizontal cross-sections of the velocity field in the simulation (left) and the experiment (right), for parameters  $F = 0.73$  and  $a = 5$  cm. The arrows represent the horizontal component of the velocity field, and the colors are mapped to the magnitude of the total velocity in m/s. The resolution for the simulation is  $1152 \times 1152 \times 192$ . Data is average over 10 minutes for the simulation and 33 minutes for the experiment.

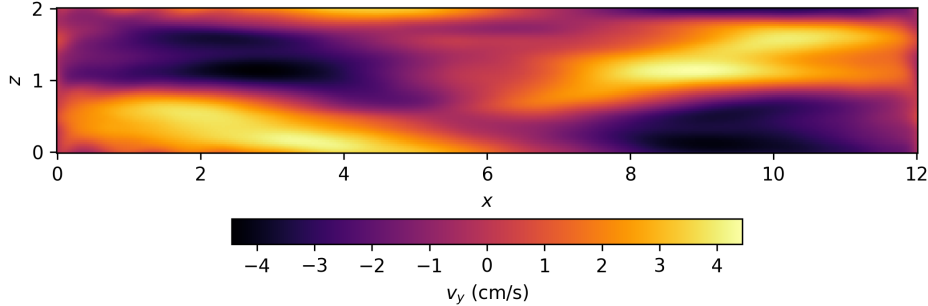


FIG. 7. Vertical cross-section going through the center of the tank ( $y = L_y/2$ ) for  $F = 0.73$ ,  $a = 5$  cm and resolution  $480 \times 480 \times 80$ . The colors show the time-averaged out-of-plane velocity.

to around sixteen hours of equation time for the simulation, meaning that the growth of the vortex mode in the experiment may not have reached saturation. In addition, because the simulation box is twice as big as the experimental domain in all directions, the vortex we observe can be twice as large as what is possible in the experiments.

The vertical structure of the mean flow is shown in figure 7. The colors show the time-averaged out-of-plane velocity for a vertical cross-section going through the center of the tank ( $y = L_y/2$ ). We see that there are actually two superposed vortices at two different levels (one vertical wavelength). This very large horizontal scale structure analogous to shear modes can most likely be interpreted as a partial condensate as defined in [31] and due to the flux loop identified in [14, 32, 33].

### C. Spatial spectra

One-dimensional spatial energy spectra are presented in figure 8. We first note that horizontal (solid lines) and vertical (dotted lines) spectra are well separated for all scales. Such strong anisotropy for all scales is typical of strongly stratified flows affected by viscosity at all horizontal scales [12]. Such flows are characterized by small buoyancy Reynolds numbers, which is consistent here as table I shows that the buoyancy Reynolds numbers measured in our simulations are typically of order unity or less. The Helmholtz decomposition of kinetic energy shows that poloidal and potential energies are equiparted at all scales, suggesting the presence of internal gravity waves. This is also indicated by the strong peak at  $k_x = k_z = 3.14$  rad/m, which corresponds to the resonant 2D modes with six horizontal wavelengths in the  $x$  direction and one wavelength in the vertical direction. The frequency of this mode is  $\omega_{6,0,1} = 0.71N$ , which is close to the forcing frequency  $\omega_f = 0.73N$ . In addition to those waves, we note that vortical energy levels are non-negligible. In fact for the vertical spectra (dotted lines), vortical energy is typically of the same order of magnitude as poloidal and potential energy, at all scales of the simulation. For the horizontal spectra, vortical energy dominates only at large scales, typically larger than the scale of the principal horizontal forcing mode  $k_x = 3.14$  rad/m, but is negligible at smaller scales.

This analysis suggests that even though waves are present at all vertical and horizontal scales, vortices still play an important role at all vertical scales, and even dominate at very large horizontal scales, which is compatible with the picture given by the horizontal mean

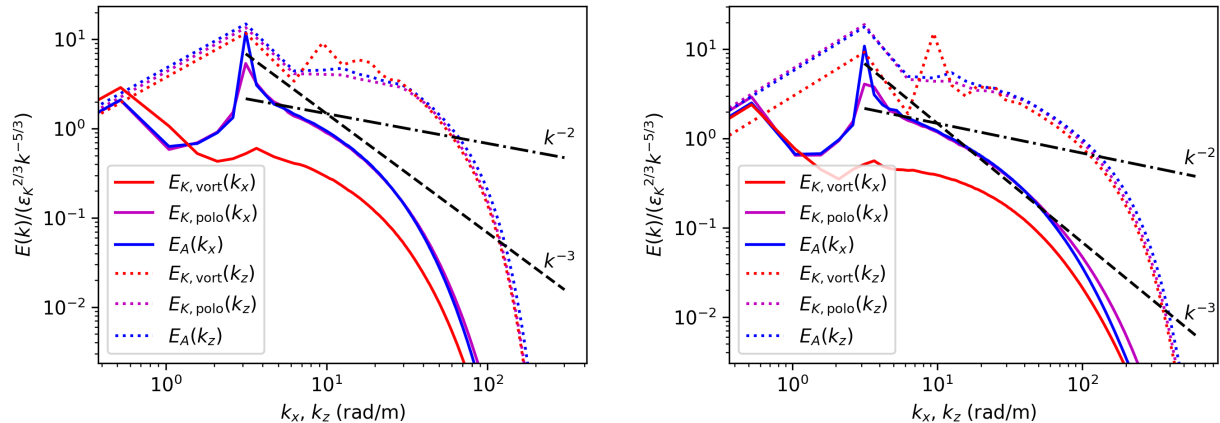


FIG. 8. One-dimensional spatial spectra for parameters  $F = 0.73$  and  $a = 5$  cm, at resolutions  $1152 \times 1152 \times 192$  (left) and  $2304 \times 2304 \times 384$  (right). All spectra are compensated by  $\varepsilon_K^{2/3} k^{-5/3}$ . Solid lines correspond to spectra along the  $x$  direction, dashed lines represent spectra along the  $z$  direction. Red curves are kinetic energy spectra, blue curves are available potential energy spectra, and purple curves represent the poloidal part of kinetic energy spectra. In black dashed and dash-dotted lines are represented power laws corresponding before compensation to  $k^{-3}$  and  $k^{-2}$ , respectively.

flow in figure 6. Finally, it should be noted that no clear scaling law appear in those spectra, whether horizontal or vertical, as shown by eye guides for  $k^{-2}$  and  $k^{-3}$  behaviors (black dashed and dashed-dotted lines). The vertical poloidal and potential energy spectra are compatible with a  $k_z^{-2}$  scaling, but on a range shorter than a decade. This absence of scaling law is probably due to the limitation of spatial resolution, as high-resolution, high- $\mathcal{R}$  2D simulations have shown such scalings to be possible [34].

#### D. Temporal spectra and linear waves relations

Similarly to what was done in [1], we present the results of a frequency analysis of the flow. All physical fields are recorded in a reduced, small-wavenumber region of Fourier space with sufficient time resolution to resolve frequencies as high as  $2N$ . Frequency spectra are then obtained by computing the Fourier transform in the temporal dimension and averaging over all recorded wavenumbers. We thus take advantage of the numerical setup, which allows us to give a more detailed frequency analysis, e.g. by computing the poloidal, vortical and potential energy spectra. The results of this analysis are presented in figure 9.

We see that all spectra show a marked peak at the forcing frequency  $F$ , signaled by a vertical, blue dashed-dotted line. Around this frequency, vortical energy is negligible and poloidal energy is equiparted with potential energy, suggesting internal gravity waves. Going down from  $F$ , the poloidal and potential energy spectra stay equal and rather flat, with the exceptions of numerous peaks at well-defined frequencies. This shape of the spectra, though quite different from the  $\omega^{-2}$  behaviour suggested by Garrett and Munk [2], is consistent with the frequency analysis of [1]. In the experimental study, peaks mostly aligned with

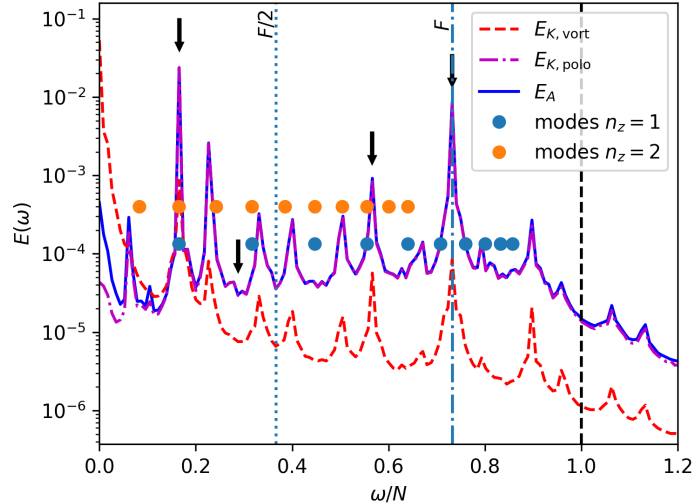


FIG. 9. Temporal spectra as a function of the normalized frequency  $\omega/N$  for parameters  $F = 0.73$  and  $a = 5$  cm, at resolution  $480 \times 480 \times 80$ . The kinetic energy spectrum is represented by the solid red line, with poloidal and vortical parts of the kinetic energy being plotted in dashed and dashed-dotted red respectively. The available potential energy spectrum is shown in solid blue. Vertical lines signal respectively the Brunt-Väisälä frequency (dashed), the forcing frequency (dashed-dotted) and half the forcing frequency (dotted). Blue dots represent the frequencies of resonant modes with  $n_z = 1$ ,  $n_y = 0$  for successive values of  $n_x$ . Orange dots represent the frequencies of resonant modes with  $n_z = 2$ ,  $n_y = 0$  for successive values of  $n_x$ . Arrows show the frequencies at which a spatio-temporal analysis is performed in figure 12.

frequencies of two-dimensional resonant modes of the tank, i.e. modes with either  $n_y = 0$  or  $n_x = 0$ . On figure 9, the frequencies of the ten first modes with  $n_y = 0$  are indicated, for  $n_z = 1$  (blue dots) and  $n_z = 2$  (orange dots). We see that only one peak is aligned clearly with modes frequencies, at  $\omega = 0.17N$  which corresponds to modes such as  $n_z = n_x$  (i.e.  $k_z = (L_x/L_z)k_x = 6k_x$ ). Other peaks fall close to other modes frequencies, but not clearly as aligned as the first peak at  $\omega = 0.17N$ , which is also the highest peaks in the spectra. In addition, we can note that all peaks below  $F$  can be associated in frequency pairs  $(\omega_a, \omega_b)$  such that  $\omega_a + \omega_b = \omega_f$ , suggesting triadic resonances with the forcing frequency. This can be intuited graphically in the representation of figure 9 with a linear scale for the frequency axis : all pairs of peaks that are symmetric with respect to  $F/2$  (signaled by a vertical, blue dotted line) verify a triadic resonance relation with the forcing. This graphical hint is then verified numerically by the calculation of the resonance relations. Such triadic resonance relations were also observed with some approximation in [1]. Finally, we note that vortical energy stays negligible until very low frequencies under  $0.1N$  where it gets larger than poloidal energy by three orders of magnitude. This is consistent with the large horizontal vortex observed in the mean flow shown in figure 6. We also note that at those frequencies, potential and poloidal energies are not equiparted anymore, suggesting that waves are absent from these scales.

The presence of internal gravity waves can be investigated further by looking for relations between spectral quantities that are verified for linear waves. We note that the linearized

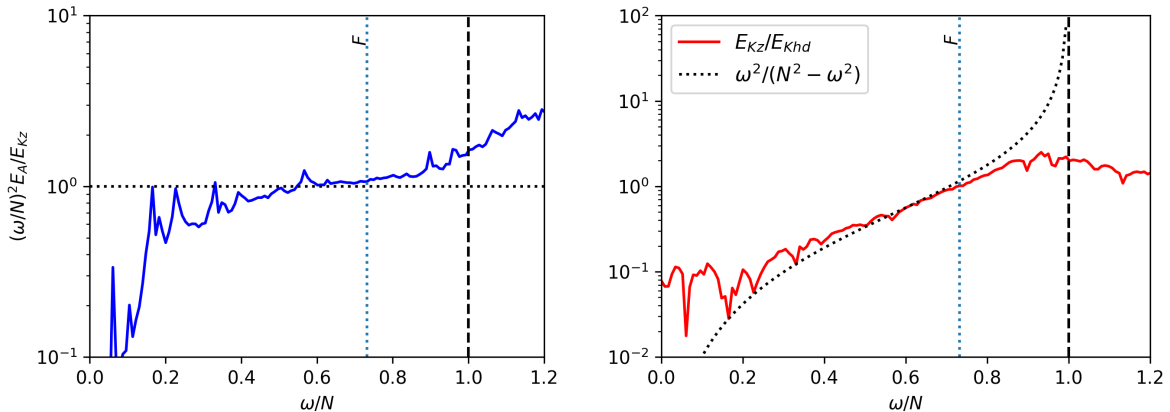


FIG. 10. Linear waves relations in  $\omega$ -space for  $F = 0.73$  and  $a = 5$  cm, at resolution  $480 \times 480 \times 80$ . Left: relation between the vertical kinetic energy and the available potential energy spectra. The horizontal dotted line represents unity. Right: relation between the vertical kinetic energy and the poloidal part of the horizontal kinetic energy spectra. The dashed curve represents the right-hand-side of equation (12). On both figures, vertical lines signal respectively the Brunt-Väisälä frequency (dashed) and the forcing frequency (dotted).

version of (2) reads:

$$\partial_t b = N^2 v_z, \quad (8)$$

which can be rewritten after taking the time Fourier transform and square modulus of each side of the equation:

$$\frac{\omega^2}{N^2} E_A(\omega) = E_{Kz}(\omega), \quad (9)$$

where  $E_A(\omega) = |\hat{b}(\omega)|^2 / (2N^2)$  and  $E_{Kz}(\omega) = |\hat{v}_z(\omega)|^2 / 2$  are the potential energy and vertical kinetic energy spectra respectively. This relation is tested in figure 10 (left), where the ratio of both sides of the equation is plotted and compared to unity. We see that relation (9) is noticeably far from being verified, though by a small amount in a short frequency range below  $F$ . Such a discrepancy should be nuanced by the fact that the set of parameters tested here corresponds to the strongest forcing used in [1], where strong mixing occurred, suggesting substantial overturning and a fortiori a regime where nonlinearities are important. In contrast, (9) is well verified at weaker forcing, for example in the experiments for  $a = 2$  cm or in simulations with different parameters presented in IV B.

Another test for the presence of linear waves would use the geometric properties of internal gravity waves. If we consider one linear wave propagating along  $\mathbf{k} = (\sin \theta \cos \phi, \sin \theta \sin \phi, \cos \theta)$ , in spherical coordinates of axis  $z$ , then the wave velocity is orthogonal to  $\mathbf{k}$  and in a vertical plane that contains  $\mathbf{k}$ . We can then decompose the velocity as an horizontal and a vertical component  $\mathbf{v} = v_h \mathbf{e}_h + v_z \mathbf{e}_z$ , such that  $\hat{v}_h(\mathbf{k}, \omega) = a(\mathbf{k}, \omega) \cos \theta$  and  $\hat{v}_z(\mathbf{k}, \omega) = a(\mathbf{k}, \omega) \sin \theta$ . Now if we assume that the flow is made of a random superposition of independent linear plane waves that are statistically axisymmetric around axis  $z$ , then the statistics of  $a$  only depend on  $k = |\mathbf{k}|$  and  $\omega$ , and we can write by taking the average power spectra of the velocity components:

$$\langle |\hat{v}_z(\mathbf{k}, \omega)|^2 \rangle = A(k, \omega) \sin^2 \theta \quad (10)$$

and

$$\langle |\hat{v}_h(\mathbf{k}, \omega)|^2 \rangle = A(k, \omega) \cos^2 \theta, \quad (11)$$

where  $A(k, \omega) = \langle |a(\mathbf{k}, \omega)|^2 \rangle$ . By summing over the azimuthal angle  $\phi$  and the wavenumber norm  $k$  we get the vertical and horizontal kinetic frequency spectra  $E_{Kz}(\omega)$  and  $E_{Kh}(\omega)$ , which share the same multiplicative factor so that their ratio reads:

$$\frac{E_{Kz}(\omega)}{E_{Kh}(\omega)} = \frac{\sin^2 \theta}{\cos^2 \theta} = \frac{\omega^2}{N^2 - \omega^2}. \quad (12)$$

Relation (12) is tested in figure 10 (right). In order to probe the wave component of the flow, the ratio  $E_{Kz}/E_{Khd}$  is shown (solid red line), where  $E_{Khd}$  is the kinetic energy associated with the divergent part of the horizontal velocity. The ratio is compared to the right hand side of equation (12). Like with equation (9), we see that the relation (12) is close to be verified in a short frequency range below the forcing, but with a significant deviation outside of this range. We note again that this relative agreement is consistent with the fact that the forcing amplitude  $a = 5$  cm corresponds to a regime where nonlinearities were observed to have a stronger effect in experiments [1].

### E. Spatiotemporal correlations

In order to probe more deeply the structure of the wave field, we perform a spatiotemporal analysis inspired by [1]. We compute the spatial correlation of velocity component  $v_i$  at fixed frequency  $\omega$  as:

$$C^{v_i}(\mathbf{x}, \omega) = \frac{\langle \hat{v}_i^*(\mathbf{x}_0 + \mathbf{x}, \omega) \hat{v}_i(\mathbf{x}_0, \omega) + \text{c.c.} \rangle}{2 \langle |\hat{v}_i(\mathbf{x}_0, \omega)|^2 \rangle}, \quad (13)$$

where  $\langle \cdot \rangle$  represents an average over  $\mathbf{x}_0$  and c.c. stands for the complex conjugate of the expression it follows. We study specifically here the vertical correlations of the horizontal velocity field, i.e. for  $v_i = v_x, v_y$  and  $\mathbf{x} = (0, dy, dz)$  lying in a vertical plane. Figure 11 show the results of this analysis in the  $dy - dz$  plane for two distinct frequencies, corresponding to the first two arrows in figure 9. The correlations for  $\omega = 0.17N$  (left column), which corresponds to a bright peak in the temporal spectra, show a large band structure with no  $dy$  dependence for  $v_x$ , and a large check pattern for  $v_y$ . The oscillations appear with one wavelength in the vertical direction for both components, and one wavelength in the  $y$  direction for  $v_y$ . These structures are thus compatible with the mode  $(n_x = 0, n_y = 1, n_z = 1)$ .

In contrast, for a frequency between peaks of the temporal spectra such as  $\omega = 0.29N$  (right column), no large-scale correlation structure emerges, but rather a cross-like pattern is visible in the correlations of  $v_y$ . The cross is highlighted by two dotted black lines with an angle  $2\theta$  between each other, with  $\theta$  being the angle associated with  $\omega = 0.29N$  through the dispersion relation. It is to be noted that this cross is observed for any frequency outside peaks of the spectra, with its angle varying accordingly with the dispersion relation. Both structures, whether on or off the peaks of the temporal spectra, are observed in experiments [1]. The on-peak correlation structure is interpreted as the presence of a two-dimensional mode in the  $y - z$  plane, whereas the off-peak cross can be interpreted as the result of the



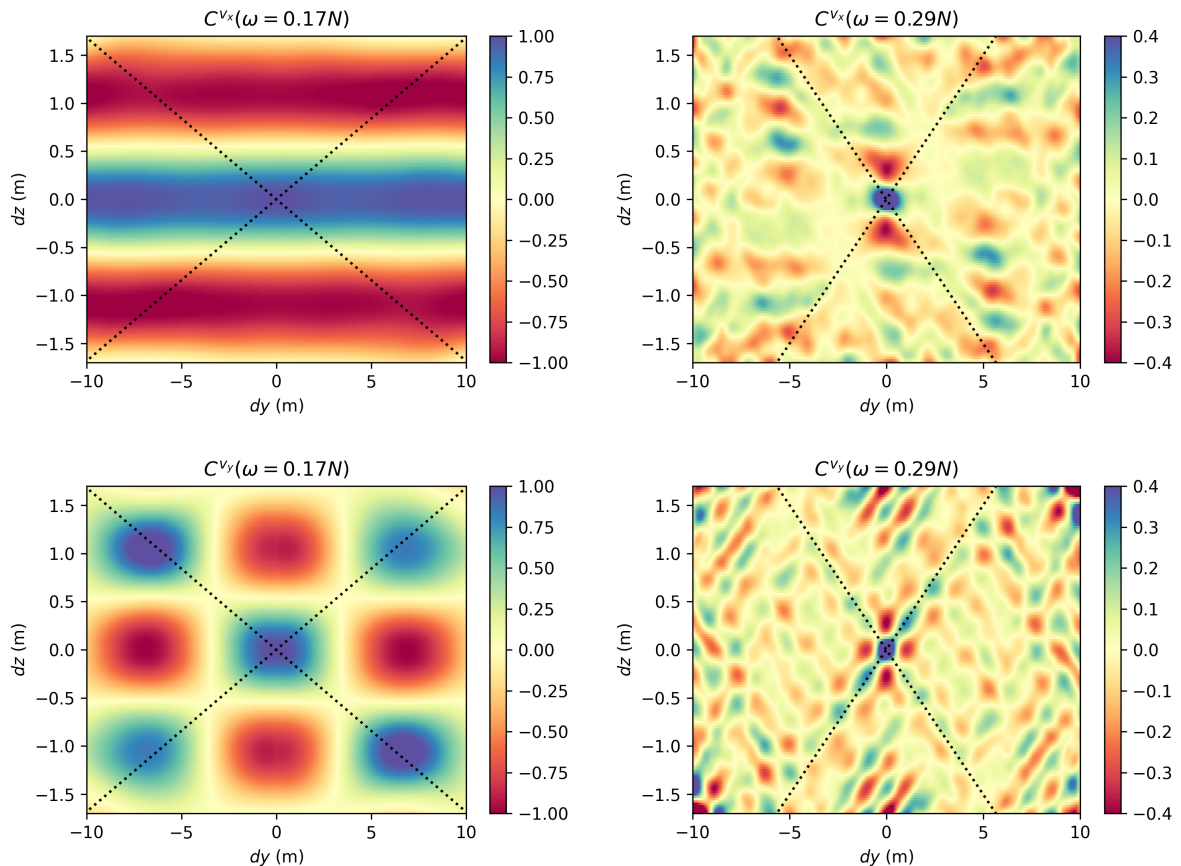


FIG. 11. Two-dimensional spatial correlations at fixed  $\omega$  of  $v_x$  (top row) and  $v_y$  (bottom row), for  $F = 0.73$  and  $a = 5$  cm, at resolution  $480 \times 480 \times 80$ . Correlations are shown at  $\omega = 0.17N$  (left column) and  $\omega = 0.29N$  (right column), which correspond respectively to the first and second arrows from the left on figure 9.

superposition of random, broadband axisymmetric waves around the vertical axis. The cross pattern we observe is less bright than in [1], however this difference could be explained by the lack of statistical convergence in our analysis, due to the shorter time over which the temporal Fourier transform is computed. Indeed, the results presented in figure 11 come from a single time window of twenty minutes of equation time, whereas in [1] a Welch method is used to average over several windows of around twenty minutes long. In addition to this lesser statistical convergence, it should again be kept in mind that the present simulation is forced with a large amplitude compared to experiments, which was associated with stronger nonlinearities and thus a less visible weak wave turbulence signature. Finally, let us note that we investigate a larger spatial window in the correlation plane, as we are able to probe a full  $12 \times 2$  m<sup>2</sup> window whereas the experimental setup of [1] only allows for a  $2.5 \times 2.1$  m<sup>2</sup> window, so the cross pattern is not observed over the same spatial scales.

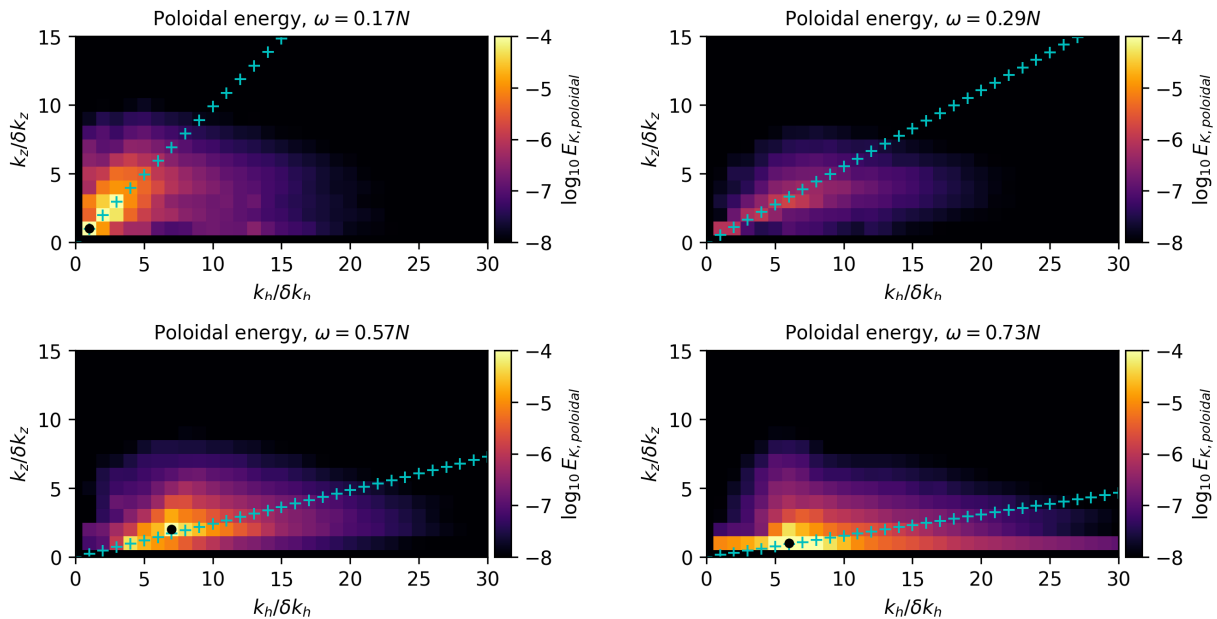


FIG. 12. Spatiotemporal spectra of poloidal kinetic energy in the  $k_z - k_h$  plane at fixed  $\omega$ , for  $F = 0.73$  and  $a = 5$  cm. Each figure corresponds to an arrow in figure 9. Top left:  $\omega = 0.17N$ . Top right:  $\omega = 0.29N$ . Bottom left:  $\omega = 0.57N$ . Bottom right:  $\omega = \omega_f = 0.73N$ . All axes are normalized by the grid spacing in its respective direction in Fourier space. Colors are mapped to the logarithm of the poloidal kinetic energy spectrum, and cyan crosses represent the internal gravity waves dispersion relation. Black dots represent the location of the energy maximum.

## F. Spatiotemporal spectra

Because the solver used for simulations is pseudospectral, the spatiotemporal analysis is more conveniently performed in spectral space rather than physical space for the spatial dimensions. In order to give a complementary point of view of the correlations picture, we performed such an analysis in  $\mathbf{k} - \omega$  space. In order to do so, we use the same technique as for the temporal spectra, which consists in saving a reduced portion of Fourier space at low  $k$ , with a sufficient time resolution. Contrary to temporal spectra however, the obtained spectra are not averaged over the whole Fourier space, so that the spatial information is not lost. Because of the anisotropic nature of stratified turbulence and internal waves, we rather perform a cylindrical average around the  $z$  axis in spectral space, in order to reduce the number of dimensions to analyze. The results of this cylindrical average are  $(2 + 1)$ -dimensional spatiotemporal spectra of the variables  $(k_h, k_z, \omega)$ .

Figure 12 shows cuts of the spatiotemporal spectra at constant  $\omega$ , which corresponds directly to the spectral equivalent of the picture of figure 11. The four panels show the poloidal energy spectra at frequencies  $\omega/N = 0.17, 0.29, 0.57, 0.73$ , which correspond to the four arrows of figure 9. The frequency  $\omega = 0.29N$  (top right) falls between peaks of the temporal spectra, whereas the three other correspond to peaks that are engaged in a triadic resonance frequency relation, with  $\omega = 0.73N$  (bottom right) being the forcing frequency and  $\omega = 0.17N$  (top left) the peak at the frequency of mode  $(n_x = 0, n_y = 1, n_z = 1)$ . We

see that for each frequency, the energy is concentrated around the internal wave dispersion relation, which is signaled by cyan plus signs. For the off-peak frequency (top right), the energy is two to three orders of magnitude lower than for the other frequencies, which is compatible with the height of the peaks that is observed in figure 9. We also note that for this frequency, the energy is distributed in a rather homogeneous manner along the dispersion relation, with no preferred wave numbers. This is different for all three on-peak frequencies, where bright peaks can be observed at rather small wavenumbers. The pixel with maximum energy is signaled by a black dot for those three frequencies. For  $\omega = 0.17N$  (top left) at  $(n_h = 1, n_z = 1)$ , for  $\omega = 0.57N$  (bottom left) at  $(n_h = 7, n_z = 2)$  and for  $\omega = 0.73N$  at  $(n_h = 6, n_z = 1)$ . It should be kept in mind that as the result of the cylindrical average around axis  $z$ , the information about the direction of  $\mathbf{k}_h$  is lost, and the simple values of  $n_h$  are not enough to validate a triadic resonance relation in  $\mathbf{k}$  space. However, a more thorough study of the spatiotemporal spectra in the  $(k_x, k_y, k_z, \omega)$  space (data not shown) shows that the maxima that are signaled by black dots actually correspond to 2D modes, namely with  $n_y = 0$ . In that case,  $\mathbf{k}_h$  coincides with  $\mathbf{k}_x$  and  $n_h$  with  $n_x$ . We thus see that the three frequencies that are engaged in a triadic resonance relation in frequency are also engaged in such relation for wavevectors, suggesting that triadic instability plays a major role in the dynamics of the flow, as observed in experiments [1].

Cuts of the spatiotemporal spectra at fixed  $k_z$  can be used to further probe the waves dispersion relation. Figure 13 show the poloidal energy spectra in the  $(k_h, \omega)$  for the three first nonzero values of  $k_z$  (i.e.  $k_z/\delta k_z = 1, 2, 3$ , with  $\delta k_z = 2\pi/L_z$ ). The energy is clearly concentrated around the dispersion relation, which is signaled again by cyan plus signs. Along the dispersion relation, frequencies that correspond to the peaks in the temporal spectra appear more energetically. When  $k_z$  increases, the dispersion relation is less visible as the energy is distributed in a wider area around it. This behaviour with  $k_z$  was also observed in [1], and is consistent with the hypothesis that small scales are more nonlinear, making the dispersion more diffuse as wavenumbers increase.

Finally, the study of vortical energy in the  $(k_h, k_z)$  plane at zero frequency, as shown in figure 14, shows high levels of energy at very large horizontal scales, and with a more extended range of vertical scales. This is compatible with the observed vortex mode in the mean flow in figure 6, and in its influence on vertical energy spectra as shown in figure 8.

## G. Spectral energy budget

Finally, we study a last aspect of the simulated flow in this first set of parameters, which is the structure of energy transfers and dissipation in spectral space. These quantities are extremely difficult to obtain experimentally. For this, we must derive the evolution equations for the kinetic and potential energy spectra  $E_K(\mathbf{k}, t)$  and  $E_A(\mathbf{k}, t)$ . This is achieved by taking the spatial Fourier transform of the equations of motion (1) and (2), multiplying them by  $\hat{\mathbf{v}}^*(\mathbf{k}, t)$  and  $\hat{b}^*(\mathbf{k}, t)$  respectively and taking the real part. The obtained equations are:

$$\partial_t E_K(\mathbf{k}, t) = T_K(\mathbf{k}, t) - C_{K \rightarrow A}(\mathbf{k}, t) - d_K(\mathbf{k}, t) + P_K(\mathbf{k}, t) \quad (14)$$

$$\partial_t E_A(\mathbf{k}, t) = T_A(\mathbf{k}, t) + C_{K \rightarrow A}(\mathbf{k}, t) - d_A(\mathbf{k}, t), \quad (15)$$

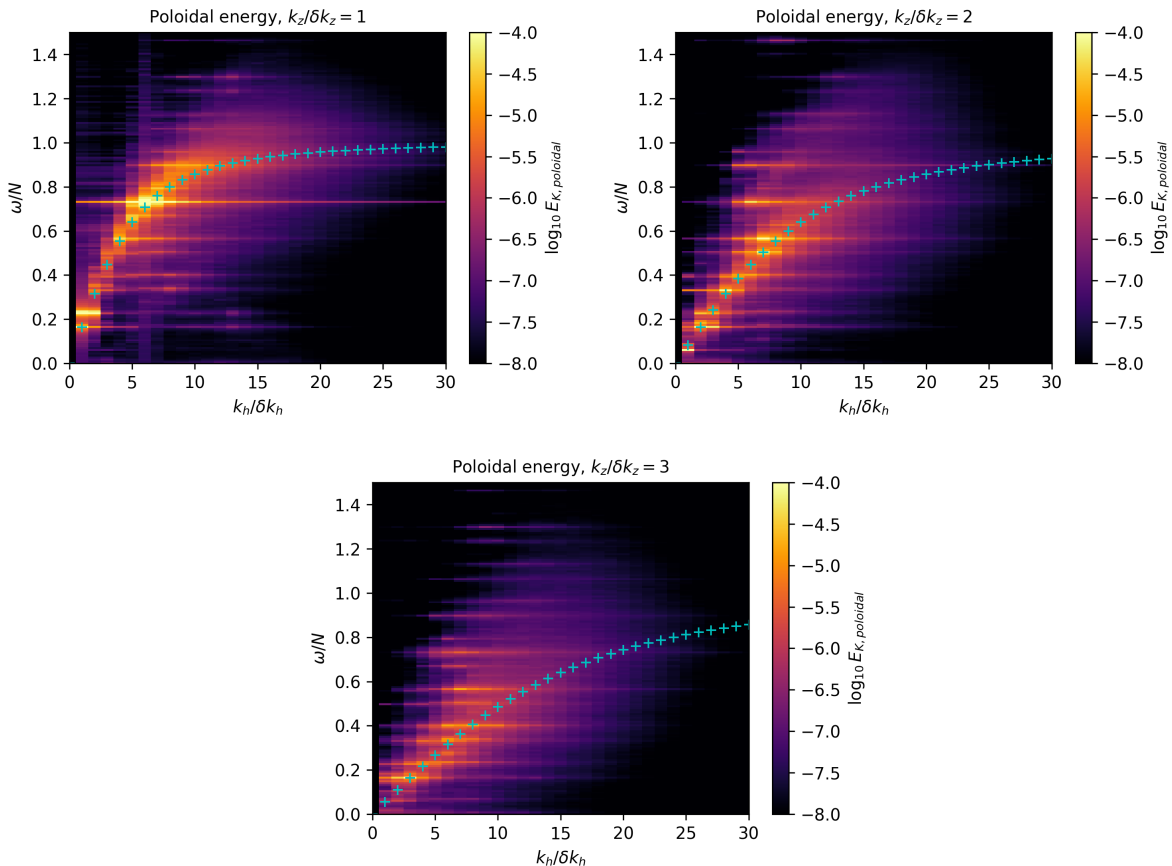


FIG. 13. Spatiotemporal spectra of poloidal energy in the  $\omega - k_h$  plane at  $k_z/\delta k_z = 1, 2, 3$ , for  $F = 0.73$  and  $a = 5$  cm, at resolution  $480 \times 480 \times 80$ . Horizontal axes are normalized by the horizontal grid spacing in Fourier space  $\delta k_h = \delta k_x = \delta k_y$ , and vertical axes are normalized by  $N$ . Colors are mapped to the logarithm of the poloidal kinetic energy spectrum, and cyan crosses represent the internal gravity waves dispersion relation.

where  $E_K(\mathbf{k}, t) = |\hat{\mathbf{v}}|^2/2$  and  $E_A(\mathbf{k}, t) = |\hat{\mathbf{b}}|^2/(2N^2)$ . The transfer terms across scales are:

$$T_K(\mathbf{k}, t) = \mathcal{R} \left[ \hat{\mathbf{v}}^* \cdot \mathbb{P}_\perp(\widehat{\mathbf{v} \times \boldsymbol{\omega}}) \right] \quad (16)$$

$$T_A(\mathbf{k}, t) = -\frac{1}{N^2} \mathcal{R} \left[ \hat{\mathbf{b}}^* \cdot \widehat{\nabla b} \right], \quad (17)$$

where  $\mathcal{R}$  denotes the real part and  $\mathbb{P}_\perp$  is the orthogonal projector onto the plane orthogonal to  $\mathbf{k}$ . By definition, we have  $\sum T_K(\mathbf{k}, t) = \sum T_A(\mathbf{k}, t) = 0$ . The conversion from kinetic to potential energy reads:

$$C_{K \rightarrow A} = -\mathcal{R} \left[ \hat{\mathbf{v}}_z^* \hat{\mathbf{b}} \right]. \quad (18)$$

Finally the power injection term is:

$$P_K(\mathbf{k}, t) = \mathcal{R} \left[ \hat{\mathbf{v}}^* \cdot \hat{\mathbf{f}} \right], \quad (19)$$

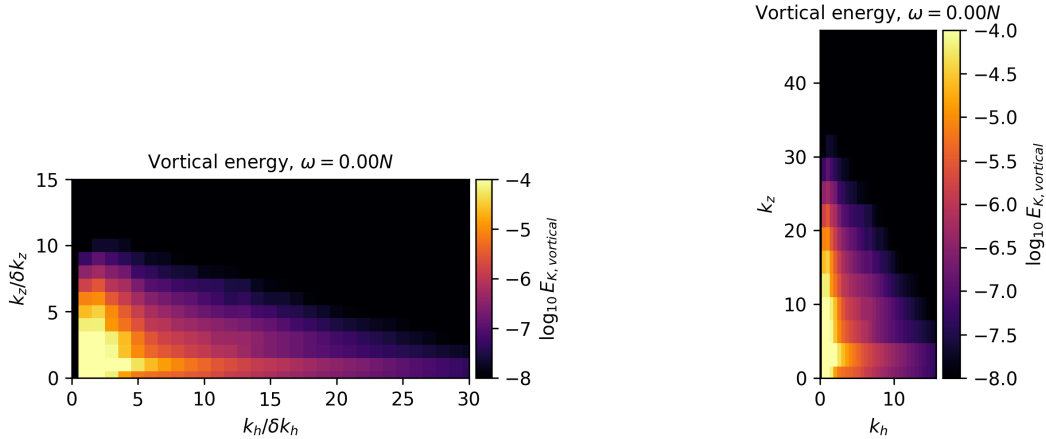


FIG. 14. Spatiotemporal spectra of vortical kinetic energy in the  $k_z - k_h$  plane at  $\omega = 0$  rad/s, for  $F = 0.73$  and  $a = 5$  cm, at resolution  $480 \times 480 \times 80$ . Left: axes are normalized by the grid spacing in Fourier space. Right: axes in dimensional units, with the same scale on the  $k_z$  and  $k_h$  axes. On both figures, the colors are mapped to the logarithm of the vortical kinetic energy spectrum.

and the dissipation terms are:

$$d_K(\mathbf{k}, t) = f_d(\mathbf{k}) E_K(\mathbf{k}, t) \quad (20)$$

$$d_A(\mathbf{k}, t) = f_d(\mathbf{k}) E_A(\mathbf{k}, t), \quad (21)$$

where  $f_d(\mathbf{k}) = \nu_2 k^2 + \nu_4 k^4$  is the dissipation frequency, equal for both types of energy as we chose  $\text{Pr}_2 = \text{Pr}_4 = 1$ . The equations (14) and (15) are called the spectral energy budget equations. In stationary state, the time derivatives of both energy types are zero in average, and the statistics of the spectral quantities in the left hand side of equations (14) and (15) do not depend on time. We therefore compute the transfer and dissipation terms of the spectral energy budget and average them over the length of the time window for the run at resolution  $1152 \times 1152 \times 192$ . The results are also summed over  $k_z$ , and integrated along  $k_h$  in order to get the horizontal spectral fluxes  $\Pi_{K,A} = \int_0^{k_h} T_{K,A}(k'_h) dk'_h$  and cumulative dissipations  $D_{K,A} = \int_0^{k_h} d_{K,A}(k'_h) dk'_h$ .

The obtained quantities are shown in figure 15 (left). Contrary to what we would expect in the picture of a direct energy cascade towards the small scales, which would be a constant energy flux between the forcing and dissipative scales, we rather observe a peculiar shape of the fluxes terms. Indeed, the negative kinetic energy flux (solid red line) at large scales indicates an average transfer towards the largest scales, whereas the positive flux above the forcing indicates a slight transfer towards the small scales. Such shape of the energy fluxes, exhibiting two separated flux loops, were already observed in 2D simulations of stratified turbulence [33, 34]. In addition, we show the behaviour of the sum of the total flux and dissipation (black dotted line), which should be constant in stationary state out of the range of scales where the forcing acts. We see here that this sum is hardly constant above the dissipative scales, indicating either that the system is not perfectly stationary or that the forcing is still acting at those scales. Note that the forcing being oscillatory, and not random, the system cannot be strictly stationary. A more thorough study of the time evolution of

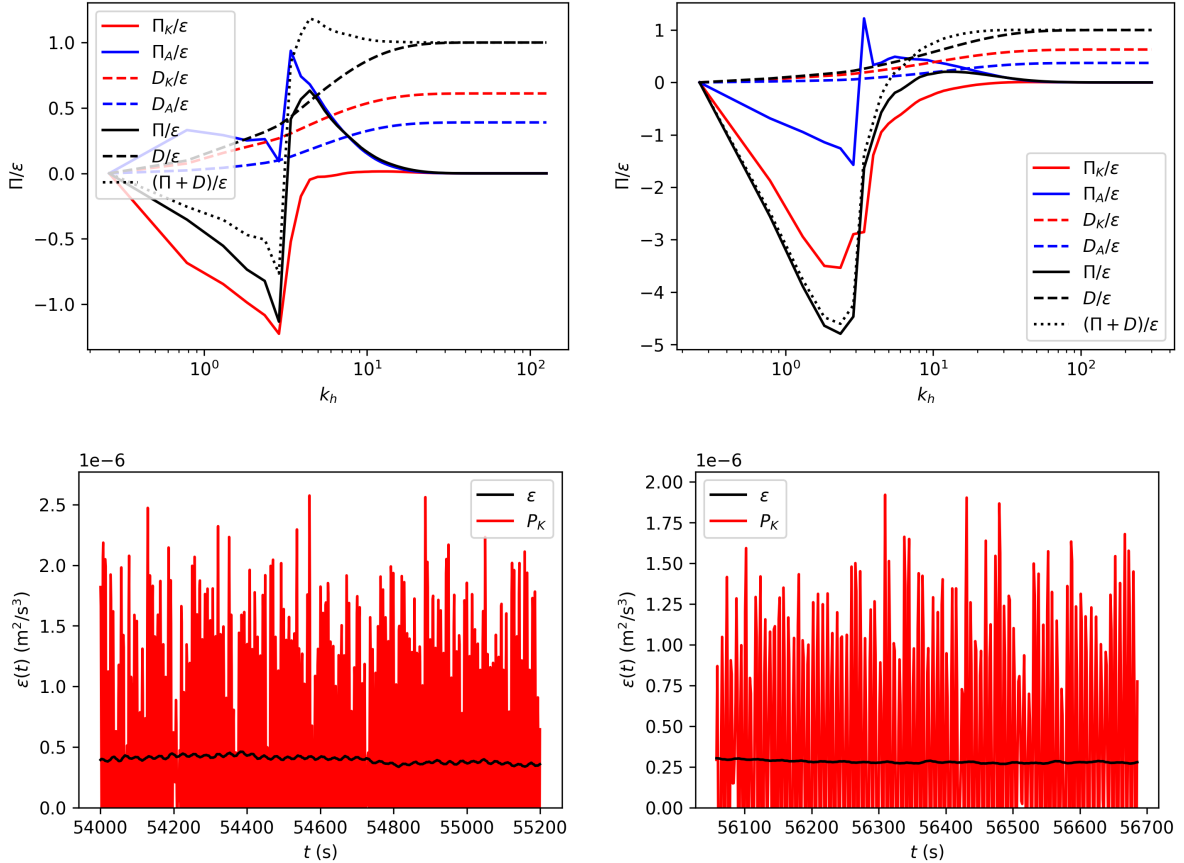


FIG. 15. Top: spectral energy budget for  $F = 0.73$  and  $a = 5$  cm, at resolutions  $480 \times 480 \times 80$  (left) and  $1152 \times 1152 \times 192$  (right). Solid red, blue and black lines are respectively the kinetic, potential and total energy fluxes. Positive values represent fluxes towards the small scales, and negative values towards the large scales. Dashed red, blue and black lines are respectively the kinetic, potential and total cumulative dissipations. The dotted black line represent the sum of the total energy flux and total cumulative dissipation. Bottom : time evolution of the total energy dissipation (solid black) and injection (dashed red) for the same simulations.

spatial spectra (data not shown) shows that the statistical stationarity is satisfying, thus suggesting that the forcing term is the more probable cause of the peculiar shape of the total flux and dissipation. Indeed, it must be recalled that the forcing scheme used here is local in space and has no preferred horizontal scale. We therefore do not expect the influence of the forcing terms to be local in spectral space. The picture drawn by the left panel of figure 15 rather suggests that the forcing term used here acts in a complicated manner over a large range of scales, which is still not well separated from the dissipative scales at this resolution. In particular, the decrease of the sum of the total flux and dissipation at large scales indicates that the forcing actually removes energy in average at those scales.

A time series of the power injection, shown on the right panel of figure 15 actually shows frequent negative excursions that are large compared to the mean injected power, which shows that the dissipative action of the forcing plays an important role in this type of flow.

It should be noted that this fluctuating aspect of the energy injection rate is typical of experimental setups such as the one used in [1, 35–37], where the power injection is not a controlled experimental parameter. In such experimental systems the fluctuation of injected power can overcome the average by several orders of magnitude, which makes statistical convergence extremely challenging. In contrast, in numerical simulations for turbulence, the forcing scheme can easily be designed in order to impose a constant energy injection rate. However the goal of the present study was to mimic the experimental setup of [1], in order to try and reproduce the results and give a complementary description of the studied flows. As a consequence, we do not control the power injection here, thus it is left to fluctuate as shown by the right panel of figure 15.

## IV. EXPLORATION OF OTHER REALISTIC PARAMETERS

### A. Stronger forcing for $F = 0.73$ : $a = 10$ cm

The simulations that are presented in section III, though close to the experiments in terms of parameters, correspond to a regime of low buoyancy Reynolds numbers, as both second and fourth order buoyancy Reynolds numbers stay slightly smaller than unity. In order to explore regimes at higher buoyancy Reynolds number, we performed another set of simulations with a stronger forcing, namely using a forcing amplitude of ten centimeters. As shown on table I, doubling the amplitude like so increases the nonlinearity while keeping Froude numbers of the order of  $10^{-3}$ , allowing for higher buoyancy Reynolds numbers such as  $\mathcal{R}_2 \simeq 5$ . Experimentally, ten centimeters was the maximum amplitude value that was tried during the study described in [1]. However, this experiment was not included in the article because of the strong mixing of salt leading to the quick destruction of the average stratification in the tank. In the present simulations the Brunt-Väisälä frequency is a fixed parameter, implying that the linear average stratification is not subject to mixing. As a consequence, the forcing amplitude could practically be set to values larger than ten centimeters in our simulations, but we choose in the present study to limit ourselves to  $a = 10$  cm in order to stay into regimes that are comparable with the experiments.

Figure 16 shows the evolution of energy components and dissipation for two runs at  $a = 10$  cm, at resolutions  $480 \times 480 \times 80$  (left) and  $1152 \times 1152 \times 192$  (right). We note that total energy levels are roughly three times higher than when forcing at  $a = 5$  cm, and total dissipation levels are one order of magnitude higher. This should be expected, as forcing with a larger amplitude means injecting more energy into the flow. However, the repartition of energy between components is more unexpected, as vortical energy levels now represent a much higher share of the total kinetic energy, with up to 80% of kinetic energy being vortical energy, compared to around 50% for  $a = 5$  cm. As shown in table I, the simulations for this stronger forcing are still very strongly stratified ( $F_h \simeq 2 \times 10^{-3}$ ) but compared to the weaker forcing ( $\mathcal{R} \simeq 0.5$ ) the buoyancy Reynolds number is now larger than 1 ( $\mathcal{R} \simeq 6$ ). Therefore, we can expect to see hints of a transition which could happen for  $\mathcal{R} \gtrsim 10$ , as in strongly stratified turbulence forced by vortices [12].

Snapshots of the buoyancy field are displayed in figure 17. Compared to figure 5, the small scale structure appear much stronger, in particular at the periphery of the numerical

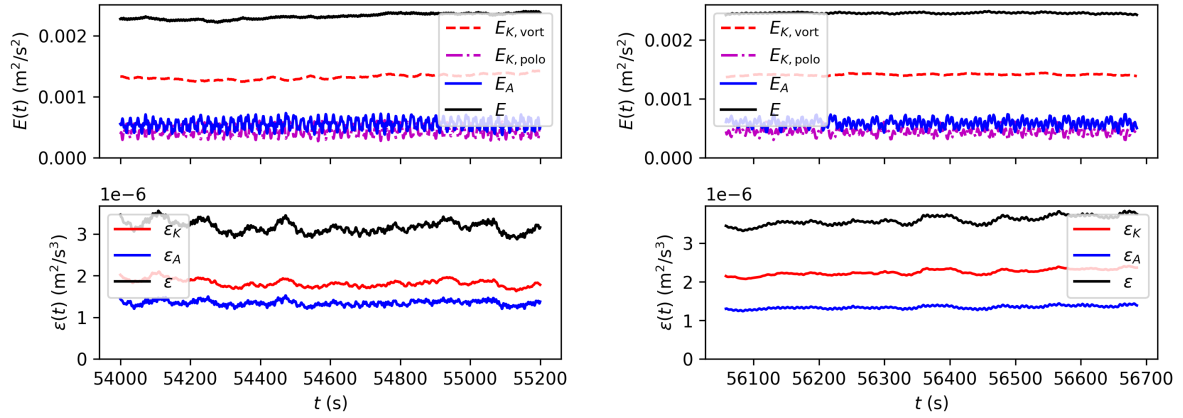


FIG. 16. Time evolution of the energy components (top row) and dissipation (bottom row) for parameters  $F = 0.73$  and  $a = 10$  cm. Data are shown for two different resolutions :  $480 \times 480 \times 80$  (left column) and  $1152 \times 1152 \times 192$  (right column), over a statistically stationary period.

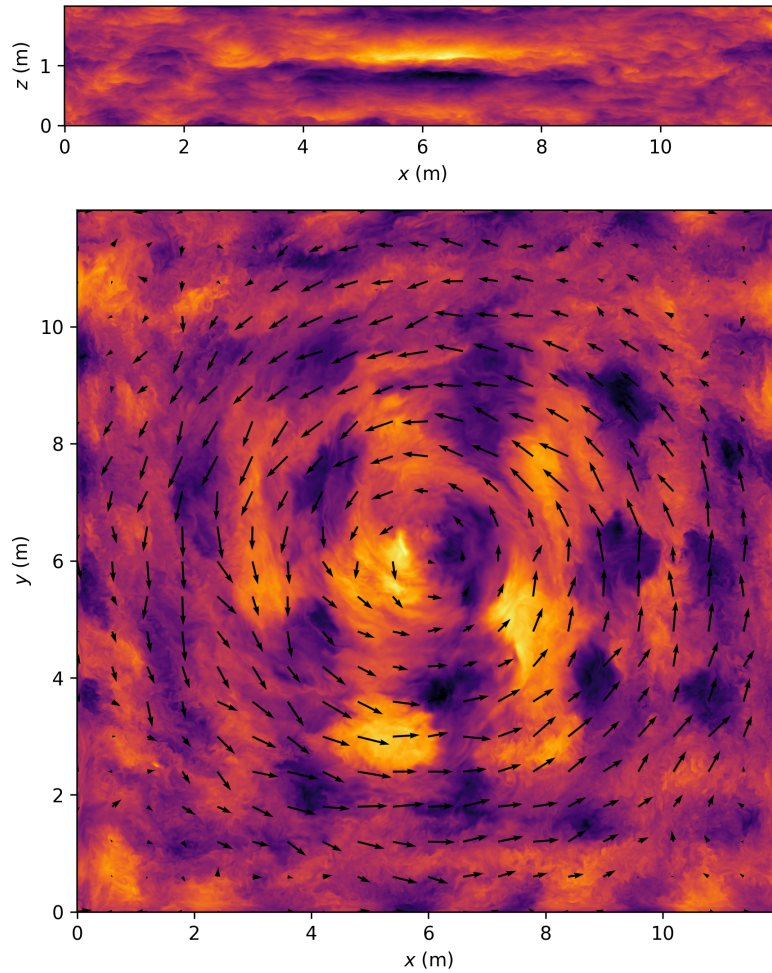


FIG. 17. Vertical (top) and horizontal (bottom) cross-sections. Same as figure 5 ( $F = 0.73$ ) but for  $a = 10$  cm. The resolution is  $2304 \times 2304 \times 384$ .



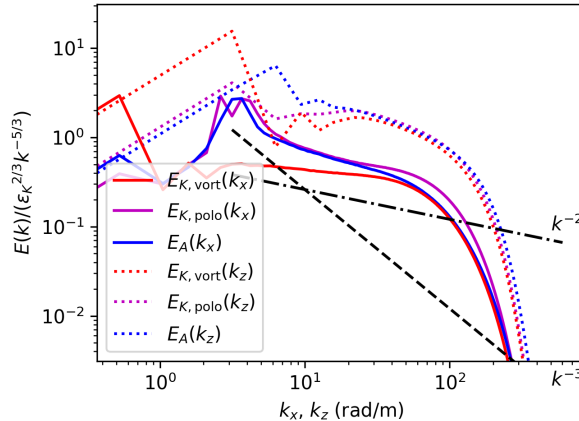


FIG. 18. One-dimensional compensated spatial spectra. Same as figure 8 ( $F = 0.73$ ) but for  $a = 10$  cm, at resolution  $2304 \times 2304 \times 384$  ( $\eta k_{\max} = 0.46$ ).

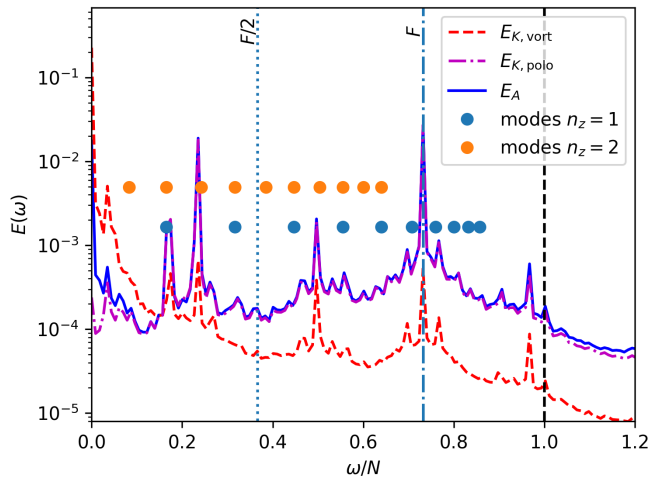


FIG. 19. Temporal spectra as a function of the normalized frequency  $\omega/N$ . Same as figure 9 but for parameters  $F = 0.73$  and  $a = 10$  cm, at resolution  $480 \times 480 \times 80$ .

domain. The velocity field is even more dominated by the horizontal vortices.

The compensated spatial spectra are shown in figure 18. The horizontal and the vertical spectra are also very different, corresponding to strongly anisotropic flows. The horizontal spectrum of vortical energy (red solid curve) is nearly flat over more than one decade. This  $k_h^{5/3}$  scaling law is consistent with a transition to a regime similar to the LAST regime at higher buoyancy Reynolds number. However, the LAST regime is associated with equal poloidal and vortical horizontal spectra, which is not observed here. This might be a finite buoyancy Reynolds number effect since these two spectra are indeed nearly equal at the smallest scales.

We show in figure 19 the temporal spectra for the run with  $a = 10$  cm and resolution  $480 \times 480 \times 80$ . The overall aspect of temporal spectra is similar to what was observed for  $a = 5$  cm (figure 9), with poloidal and potential energy dominating above  $\omega = 0.2N$ ,

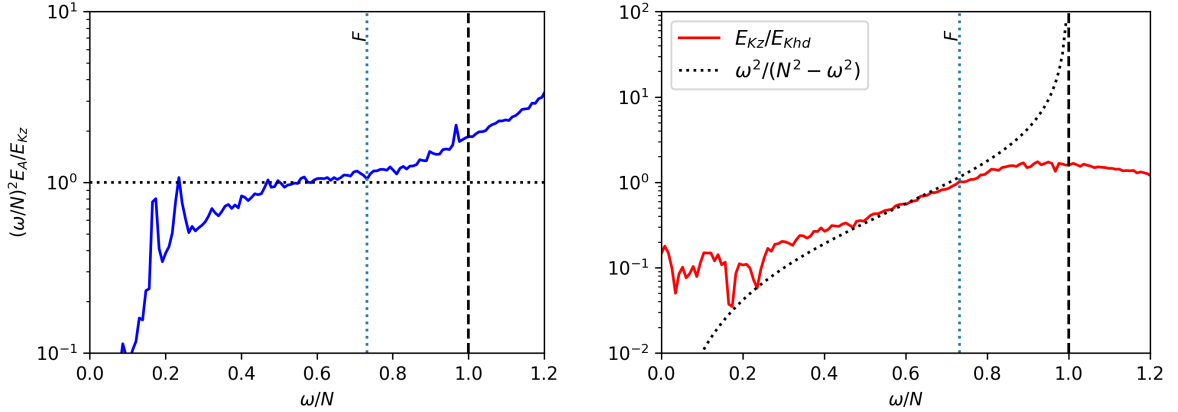


FIG. 20. Linear waves relations in  $\omega$ -space. Same as figure 10 but for  $F = 0.73$  and  $a = 10$  cm, at resolution  $480 \times 480 \times 80$ .

both spectra staying quite close to each other and showing rather constant levels below the forcing frequency, except for a few sharp peaks. Differences can be seen first in the number of peaks, as fewer peaks are observable than for  $a = 5$  cm. The off-peak energy continuum of axisymmetric waves increases faster than the peaks level, as observed in experiments when increasing the forcing amplitude [1]. A second difference lays in the slight offset between poloidal and potential energy around  $F/2$  (dotted vertical line), which was almost not observable for  $a = 5$  cm. This larger offset suggests that waves dynamics are departing from mostly linear interaction. Finally, the vortical energy levels at very low frequency are also different from what was observed in figure 9: the extension of the frequency range where vortical energy dominates is larger, with vortical energy remaining non-negligible up to the first peak in the poloidal/potential energy spectra. These higher vortical energy levels at very low frequencies suggests that the increase in the share taken by vortical energy corresponds to a relative growth of the slow vortex mode that was observed in figure 6.

The study of characteristic relations (9) and (12), as presented on figure 20, shows that linear wave dynamics are less at play here than for  $a = 5$  cm, which is consistent with higher levels of nonlinearity due to a stronger energy injection into the system.

Figure 21 (left) shows a cut of the poloidal energy spatiotemporal spectrum in the  $k_h - \omega$  plane, for the first value of  $k_z$  (i.e. for  $k_z/\delta k_z = 1$ ). We see that the energy remains maximal on the dispersion relation (cyan plus signs), though it is distributed in a wider region around the relation. This is compatible with the higher levels of nonlinearity that were suggested by the temporal analysis. Note also that the spread of energy around the dispersion relation is wider at higher  $k_h$ , suggesting that the flow is strongly non linear at small scales.

## B. Slower forcing

In all simulations presented in previous sections, we observe the generation of internal gravity waves at frequencies below the forcing. In order to also study the behaviour of waves above the forcing, we perform a final set of simulations with a lower normalized forcing frequency, namely  $F = 0.4$ . Because the velocity of the oscillating panel of the forcing

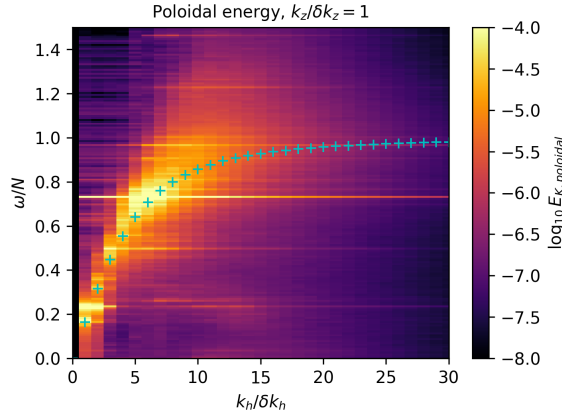


FIG. 21. Spatiotemporal spectrum of poloidal kinetic energy. Same as figure 13, but for  $F = 0.73$  and  $a = 10$  cm, at resolution  $480 \times 480 \times 80$ . The spectrum is shown in the  $\omega - k_h$  plane at  $k_z/\delta k_z = 1$ .

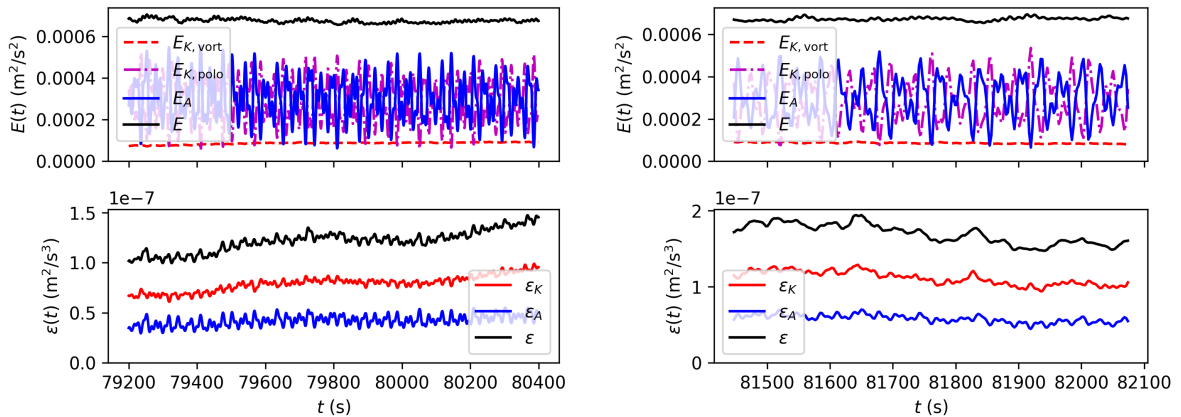


FIG. 22. Time evolution of the energy components (top row) and dissipation (bottom row) for parameters  $F = 0.73$  and  $a = 10$  cm. Data are shown for two different resolutions :  $480 \times 480 \times 80$  (left column) and  $1152 \times 1152 \times 192$  (right column), over a statistically stationary period.

mechanism is proportional to the motion amplitude  $a$  and frequency  $F$ , the reduction of the forcing frequency induces a decrease of the power injection into the flow. Simulations with  $F = 0.4$  and  $a = 5$  cm have been performed (data not shown), though the power injection in this setup was too inefficient to obtain regimes of dynamics that were comparable to the previous parameters sets. In order to compensate the decrease of the forcing frequency, the amplitude is also increased to  $a = 10$  cm.

Figure 22 shows the evolution of energy components and dissipations for resolution  $480 \times 480 \times 80$  and  $1152 \times 1152 \times 192$ . Total energy and dissipation levels are slightly lower than for  $F = 0.73$  and  $a = 5$  cm, indicating that the forcing mechanism is injecting slightly less power into the flow. We also note that the relative level of vortical energy is smaller, with vortical energy accounting for around 30% of all kinetic energy.

Frequency spectra are shown in figure 23. The overall aspect of spectra is similar to

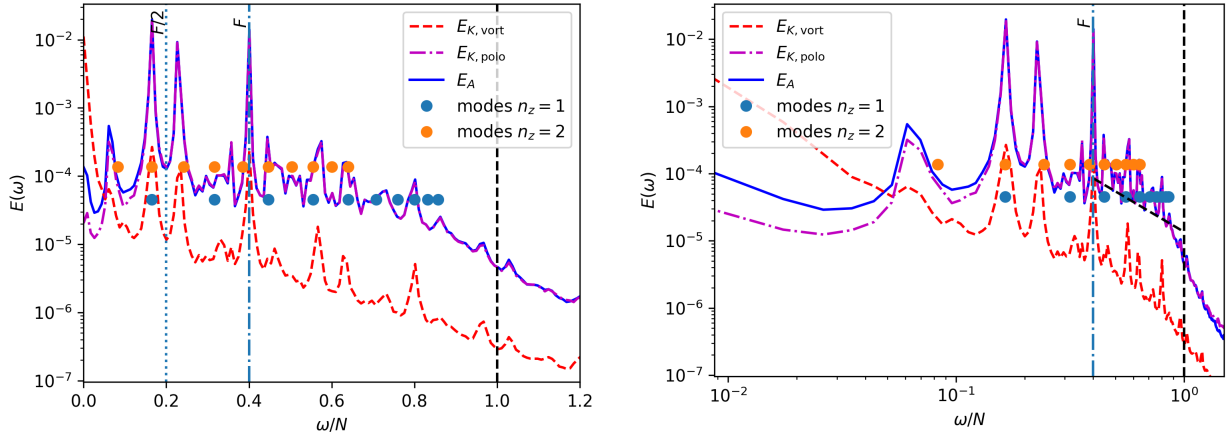


FIG. 23. Temporal spectra as a function of the normalized frequency  $\omega/N$ . Same as figure 9 but for parameters  $F = 0.40$  and  $a = 10$  cm, at resolution  $480 \times 480 \times 80$ . Right: logarithmic scale, with the  $\omega^{-2}$  scaling plotted as a black dashed line between  $\omega = \omega_f$  and  $\omega = N$ .

what was observed in the previous cases, though the frequency range between  $F$  and  $N$  is now larger. Below the forcing, poloidal (dashed red) and potential (solid blue) energy levels are very close to each other, suggesting linear waves. Toroidal energy is negligible down to very low frequencies below  $\omega = 0.1N$ , which represents a lower limit than for  $a = 5$  cm, showing that the lower levels of vortical energy are associated with a smaller frequency range of action. In all spectral components, fewer peaks can be observed than for  $a = 5$  cm, though the three most visible peaks correspond to frequencies that are engaged in a triadic resonance relation  $\omega_a + \omega_b = \omega_c$ , where  $\omega_a = 0.17N$  is again the frequency of 2D resonant modes such that  $n_x = 0$ ,  $n_y = n_z$ ,  $\omega_b = 0.23N$  and  $\omega_c = \omega_f = 0.40N$ . We note that a triadic resonance relation involving both the forcing frequency and the frequency of 2D modes such that  $n_h = n_z$  is always observable in all simulations that were performed. This was confirmed by using a slightly faster forcing frequency  $F = 0.45$  with the same amplitude (see table I), showing that the same triadic relation was verified between the forcing, the first resonant 2D mode and a third frequency  $\omega_b = 0.28N$  (data not shown). Above the forcing frequency, poloidal and potential energy are again very close, indicating that linear internal waves are also generated at those frequencies. We observe less marked peaks in this range, and a logarithmic scale representation (left panel of figure 23) shows that the spectral behaviour at those frequencies is compatible with a  $\omega^{-2}$  Garrett and Munk spectrum [2]. A qualitatively similar spectrum could be described in experiments [15].

Figure 24 shows the study of linear waves relations (9) and (12). We observe a good agreement with linear waves dynamics in an extended frequency range, which is consistent with a less energetic flow than for  $F = 0.73$  and  $a = 5$  cm.

The results of spatiotemporal analysis are shown on figure 25, where the poloidal energy spectra are shown in the  $k_h - k_z$  plane for different frequencies. The three frequencies corresponding to the triadic resonance relation are shown, as well as one off-peak frequency at  $\omega = 0.29N$ . For the three on-peak spectra, the maximum of energy is shown by a black dot. In contrast to the case where  $a = 5$  cm, the wavenumber values corresponding to energy maxima cannot be interpreted as being involved in one triadic resonance relation. To explain

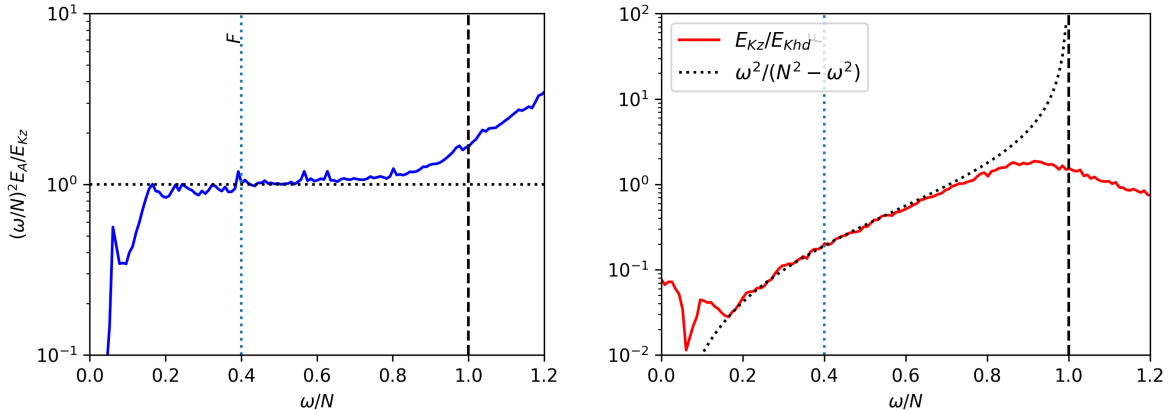


FIG. 24. Linear waves relations in  $\omega$ -space. Same as figure 10 but for  $F = 0.40$  and  $a = 10$  cm, at resolution  $480 \times 480 \times 80$ .

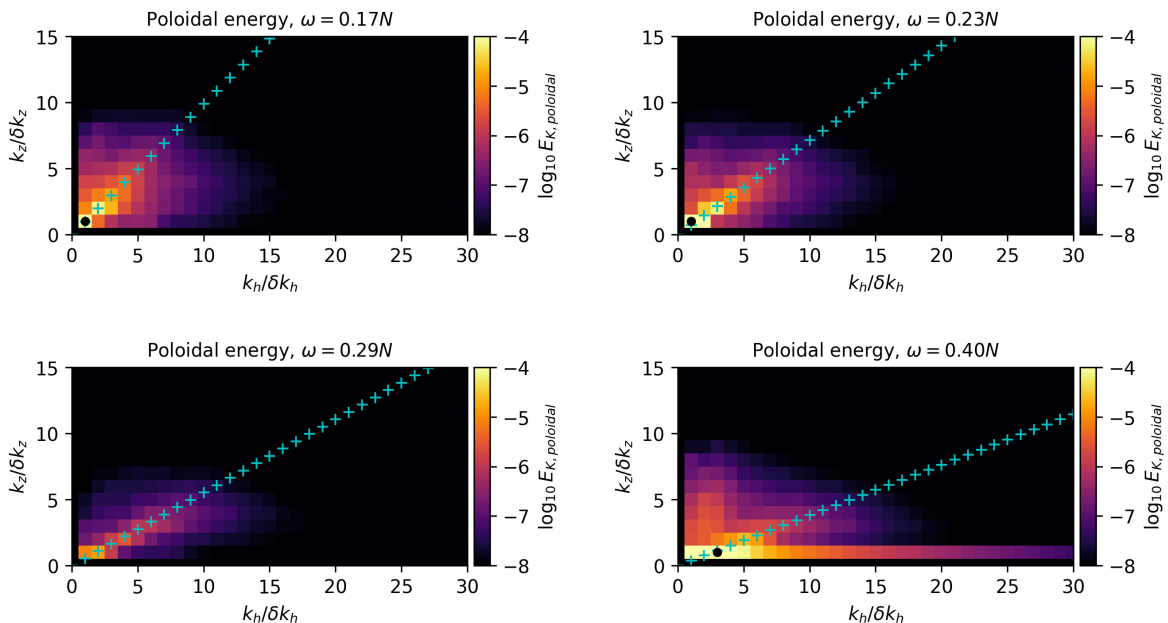


FIG. 25. Spatiotemporal spectra of poloidal kinetic energy in the  $k_z - k_h$  plane at fixed  $\omega$ . Same as figure 12 but for  $F = 0.40$  and  $a = 10$  cm. Each figure corresponds to an arrow in figure 9.

the energy repartition for these 3 frequencies, one needs to consider more modes and few nearly resonant triads.

Figure 26 shows a cut of the spatiotemporal poloidal energy spectrum in the  $k_h - \omega$  plane, for the first value of  $k_z$ . We see that the energy is concentrated around the dispersion relation, with a smaller width than for  $F = 0.73$  and  $a = 5$  cm. This closer repartition of energy with respect to the dispersion relation is consistent with more linear waves dynamics in a regime where the power injection into the flow is smaller. It is qualitatively consistent with a regime of weak wave turbulence. Forcing with a more adapted scheme may allow one

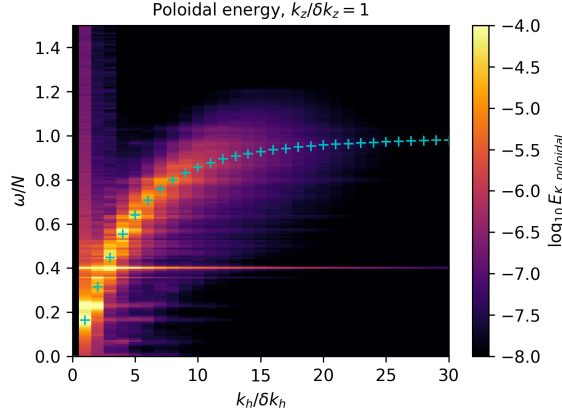


FIG. 26. Spatiotemporal spectrum of poloidal kinetic energy. Same as figure 13, but for  $F = 0.40$  and  $a = 10$  cm, at resolution  $480 \times 480 \times 80$ . The spectrum is shown in the  $\omega - k_h$  plane at  $k_z/\delta k_z = 1$ .

to observe a GM spectrum at lower frequency.

## V. CONCLUSIONS AND PERSPECTIVES

We performed numerical simulations of a stratified turbulent flow, using a forcing mechanism inspired by experiments done in the Coriolis facility [1, 15]. The generated flows exhibited turbulent Froude numbers around  $10^{-3}$  and buoyancy Reynolds numbers ranging from 0.22 to 6.3. Using realistic parameters, we were able to reproduce some key elements of the experimental flows. Internal gravity waves are observed at all frequencies  $\omega < N$  and mainly at large scales, where they interact in a weak nonlinear fashion. The increase in power injection is shown to reduce the range of observable linear waves, which is consistent with experiments and the standard phenomenology of stratified turbulence. A spectral analysis enables us to reproduce the spatiotemporal structure of the motion that was observed in experiments, especially the peculiar shape of temporal spectra below the forcing frequency, made of a flat continuum and several marked peaks. The discrete frequencies of the peaks are shown to be involved in triadic resonance relations with the frequencies of the forcing and a few large scale resonant modes.

A more detailed spatiotemporal analysis has evidenced new aspects of the studied flows. Vortical energy is shown to condensate at the largest scales in both space and time, resulting in a strong mean flow that takes the form of a large horizontal vortex the size of the simulation domain. The relative part of kinetic energy that is taken up by the vortex, as well as the frequency range at which it acts, are shown to increase strongly with the power injection from the forcing. This vortical flow could be linked to the nature of the specific forcing scheme that was used, which was shown to have complex dynamics in both space and time, injecting and dissipating energy at both large and intermediate scales.

Finally, using a lower forcing frequency, it was shown that weakly nonlinear waves are also generated above the forcing frequency, with a structure that is not incompatible with a  $\omega^{-2}$  Garrett and Munk spectrum. However, we also found that some other key elements

from the standard phenomenology of inertial range turbulent cascades, such as constant energy fluxes through scales or power law spectra behaviour, were absent from the studied flow. This is coherent with both the presence of waves mainly at large scales and with the anisotropy of spatial energy spectra. All those observations are typical of viscosity-affected stratified flows, which are characterized by small buoyancy Reynolds numbers. Indeed, the flows that we studied here, which were parametrized to mimic experimental flows, exhibit buoyancy Reynolds numbers of the order of unity or less, suggesting regimes at the transition between viscosity-affected stratified flows and strongly stratified turbulence. Regimes at higher buoyancy Reynolds numbers were explored in 2D in other numerical works [34], and showed the presence of an actual inertial turbulent range.

Further studies should be aimed in the future at a better understanding of the peculiar forcing that was used in this article and in [1, 15], as well as its relation to the growth of the large scale vortical flow.

### ACKNOWLEDGMENTS

This research was funded, in whole or in part, by the European Research Council (ERC) under the European Union's Horizon 2020 research and innovation program (Grant No. 647018-WATU). A CC-BY public copyright license has been applied by the authors to the present document and will be applied to all subsequent versions up to the Author Accepted Manuscript arising from this submission, in accordance with the grant's open access conditions. It was also partially supported by the Simons Foundation through the Simons collaboration on wave turbulence. Part of this work was performed using resources provided by CINES under GENCI allocation number A0080107567.

- 
- [1] C. Savaro, A. Campagne, M. C. Linares, P. Augier, J. Sommeria, T. Valran, S. Viboud, and N. Mordant, Generation of weakly nonlinear turbulence of internal gravity waves in the coriolis facility, *Phys. Rev. Fluids* **5**, 073801 (2020).
  - [2] C. Garrett and W. Munk, Internal waves in the ocean, *Annual review of fluid mechanics* **11**, 339 (1979).
  - [3] M. E. McIntyre, Balanced flow, *Encyclopedia of Atmospheric Sciences* **2**, 680 (2003).
  - [4] M. L. Waite and P. Bartello, Stratified turbulence generated by internal gravity waves, *J. Fluid Mech.* **546**, 313 (2006).
  - [5] P. Caillol and V. Zeitlin, Kinetic equations and stationary energy spectra of weakly nonlinear internal gravity waves, *Dynamics of atmospheres and oceans* **32**, 81 (2000).
  - [6] K. L. Polzin and Y. V. Lvov, Toward regional characterizations of the oceanic internal wave-field, *Reviews of geophysics* **49** (2011).
  - [7] E. Lindborg and G. Brethouwer, Stratified turbulence forced in rotational and divergent modes, *J. Fluid Mech.* **586**, 83 (2007).
  - [8] J. J. Riley and E. Lindborg, Stratified turbulence: A possible interpretation of some geophysical turbulence measurements, *Journal of the Atmospheric Sciences* **65**, 2416 (2008).
  - [9] E. Lindborg, The energy cascade in a strongly stratified fluid, *J. Fluid Mech.* **550**, 207 (2006).

- [10] S. M. de Bruyn Kops and J. J. Riley, The effects of stable stratification on the decay of initially isotropic homogeneous turbulence, *J. Fluid Mech.* **860**, 787 (2019).
- [11] G. D. Portwood, S. M. de Bruyn Kops, J. R. Taylor, H. Salehipour, and C. Caulfield, Robust identification of dynamically distinct regions in stratified turbulence, *J. Fluid Mech.* **807** (2016).
- [12] G. BRETHOUWER, P. BILLANT, E. LINDBORG, and J.-M. CHOMAZ, Scaling analysis and simulation of strongly stratified turbulent flows, *J. Fluid Mech.* **585**, 343–368 (2007).
- [13] T. Le Reun, B. Favier, and M. Le Bars, Parametric instability and wave turbulence driven by tidal excitation of internal waves, *J. Fluid Mech.* **840**, 498 (2018).
- [14] M. Calpe Linares, Numerical study of 2D stratified turbulence forced by internal gravity waves, Ph.D. thesis, Université Grenoble Alpes (2020), co-directed by P. Augier and N. Mordant.
- [15] C. Rodda, C. Savaro, G. Davis, J. Reneuve, P. Augier, J. Sommeria, T. Valran, S. Viboud, and N. Mordant, Experimental observations of internal wave turbulence transition in a stratified fluid, *Phys. Rev. Fluids* **7**, 094802 (2022).
- [16] P. Augier, A. V. Mohanan, and C. Bonamy, FluidDyn: A python open-source framework for research and teaching in fluid dynamics by simulations, experiments and data processing, *Journal of Open Research Software* **7**, 10.5334/jors.237 (2019).
- [17] A. V. Mohanan, C. Bonamy, and P. Augier, FluidFFT: Common API (c++ and python) for fast fourier transform HPC libraries, *Journal of Open Research Software* **7**, 10.5334/jors.238 (2019).
- [18] A. V. Mohanan, C. Bonamy, M. C. Linares, and P. Augier, FluidSim: Modular, Object-Oriented Python Package for High-Performance CFD Simulations, *Journal of Open Research Software* **7**, 10.5334/jors.239 (2019).
- [19] <https://pypi.org/project/fluidsim/0.6.1/>.
- [20] P. Angot, C.-H. Bruneau, and P. Fabrie, A penalization method to take into account obstacles in incompressible viscous flows, *Numerische Mathematik* **81**, 497 (1999).
- [21] T. Engels, D. Kolomenskiy, K. Schneider, and J. Sesterhenn, Flusi: A novel parallel simulation tool for flapping insect flight using a fourier method with volume penalization, *SIAM Journal on Scientific Computing* **38**, S3 (2016).
- [22] J. J. Riley and M.-P. Lelong, Fluid motions in the presence of strong stable stratification, *Annual review of fluid mechanics* **32**, 613 (2000).
- [23] C. Cambon, Turbulence and vortex structures in rotating and stratified flows, *European Journal of Mechanics-B/Fluids* **20**, 489 (2001).
- [24] A. Craya, Contribution à l’analyse de la turbulence associée à des vitesses moyennes, *Pub. Sci. Tech. du Ministère de l’Air (France)* (345) (1958).
- [25] J. Herring, Approach of axisymmetric turbulence to isotropy, *Phys. Fluids* **17**, 859 (1974).
- [26] L. M. Smith and F. Waleffe, Generation of slow large scales in forced rotating stratified turbulence, *J. Fluid Mech.* **451**, 145 (2002).
- [27] P. Augier, P. Billant, and J.-M. Chomaz, Stratified turbulence forced with columnar dipoles: numerical study, *J. Fluid Mech.* **769**, 403 (2015).
- [28] A. Maffioli, A. Delache, and F. S. Godeferd, Signature and energetics of internal gravity waves in stratified turbulence, *Physical Review Fluids* **5**, 10.1103/physrevfluids.5.114802 (2020).
- [29] This is done with the parameter `params.oper.NO_SHEAR_MODES` of the `ns2d.strat` and `ns3d` Fluidsim solvers, which extends the truncation used for dealiasing to the shear modes.



- [30] Parameter `params.no_vz.kz0` in Fluidsim.
- [31] A. van Kan and A. Alexakis, Condensates in thin-layer turbulence, *Journal of Fluid Mechanics* **864**, 490–518 (2019).
- [32] A. Kumar, M. K. Verma, and J. Sukhatmae, Phenomenology of two-dimensional stably stratified turbulence under large-scale forcing, *Journal of Turbulence* **18**, 219 (2017).
- [33] G. Boffetta, F. De Lillo, A. Mazzino, and S. Musacchio, A flux loop mechanism in two-dimensional stratified turbulence, *Europhysics Letters* **95** (2011).
- [34] M. C. Linares, Numerical study of 2D stratified turbulence forced by internal gravity waves, Ph.D. thesis, Université Grenoble Alpes [2020-....] (2020).
- [35] J.-F. Pinton, P. C. Holdsworth, and R. Labbé, Power fluctuations in a closed turbulent shear flow, *Physical Review E* **60**, R2452 (1999).
- [36] O. Cadot, C. Touzé, and A. Boudaoud, Linear versus nonlinear response of a forced wave turbulence system, *Physical Review E* **82**, 046211 (2010).
- [37] S. Aumaître, E. Falcon, and S. Fauve, Fluctuations of the energy flux in wave turbulence, *Advances in Wave Turbulence* , 53 (2013).